Development of the Somali Current System During the Southwest Monsoon

by

Alex H. Meng

A thesis submitted to the
Department of Meteorology
in partial fulfillment of the
requirements for the degree of
Master of Science

Approved:

James J. O'Brien
Professor Directing Thesis

T.Y. Tsiang

Jon E. Ahlquist

December, 1984

ABSTRACT

Results are presented from two cases of a model of the seasonal circulation in the northwest Indian Ocean. The model is a nonlinear reduced gravity transport model, with realistic basin geometry and using observed winds as forcing. One case is forced by the monthly mean of the FGGE winds while the other is forced by the monthly mean climatological winds. The two cases are compared and inferences are made as to the importance of the different mechanisms at work in the generation and decay of the Somali Current system during the southwest monsoon. The Southern Hemisphere currents are shown to reverse prior to the local winds, due to the relaxation of the northeast monsoon winds. The southern gyre of the two gyre system responds primarily to the Southern Hemisphere tradewinds, while the northern gyre forms north of 4°N in response to the development of the Findlater jet and its associated wind stress curl. The two gyre system collapse is highly correlated with a decrease in the westerly component of the equatorial wind stress. The circulation patterns are strongly influenced by the gradient of the wind stress curl, as well as by the curl itself. The transition from southwest to northeast monsoon conditions depends on the remnants of the previous season's circulation patterns.

northeast monsoon conditions depends on the remnants of the previous season's circulation patterns.

ACKNOWLEDGEMENTS

I would like to express my most sincere gratitude to Dr. J. J. O'Brien for his support and guidance as my major professor. His suggestions and criticism during the course of this study were most constructive. I am also grateful of the time taken by Dr. T. N. Krishnamurti and Dr. J. E. Ahlquist while serving on my thesis committee.

In addition, sincere appreciation is extended to my colleagues in the Mesoscale Air-Sea Interaction Group for providing fruitful discussion. I am deeply indebted to Dr. Mark E. Luther for his invaluable help during the whole process of doing this thesis.

This work is an extension of an original model developed by Dr. Mark E. Luther and Dr. J. J. O'Brien. This work was supported by The Office of Naval Research. Computations were performed on the CDC 760 at the Florida State University.

I wish to thank Mrs. Helen McKelder for typing both the early draft copies and the final version of this thesis.

TABLE OF CONTENTS

LIST OF FIGURES

large wind stress builds over the northern Arabian Sea, forming the beginnings of the

Contour interval is 1.0 x 10^{-7} N m^{-3}. Labels are in units of 20^{-8} N m^{-3}.

There are two relative maxima in the Northern Hemisphere, one to the east of Socotra, and

from the FGGE case, but we still see a relative maximum in negative curl centerd at

curl, with its two branches, has intensified, but remains in approximately the same

along the equator into a broad meandering equatorial current, that is not present in the

great whirl. This jet is not seen in the FGGE case.

southeast of Socotra is beginning to meander.

Socotra, with a small cyclonic circulation

MMC case. Lines A and B follow the separation region between the southern and northern gyre. Lines C and D follow the center of the southern gyre recirculation region. Line E follows the northward movement of the great whirl. Units are 10^6 m^3 s^{-1}. Contour interval is 10 x 10^6 m^3 s^{-1}.

INTRODUCTION

Recent observations have revealed a great deal of information on the development of the Somali Current system with the onset of the southwest (SW) monsoon. The picture that has emerged is that of a complicated multiple gyre circulation pattern, with rapid transitions from one configuration to another. The Somali Current develops from a weak southward flow to a very strong northward current, with transports of more than 60×10^6 $m^3 s^{-1}$, in roughly four months. This is quite a spectacular change, especially when compared to the seasonal variations in the other oceans. Excellent reviews of the recent observational and theoretical advances in this area are given by Schott (1983) and Knox and Anderson (1984).

During northern winter, the winds over the northwestern Indian Ocean are northeasterly (the NE monsoon) and drive a southwestward boundary current along the coast of Somalia. This current meets the northward flowing East African Coastal Current (EACC), which is driven by the Southern Hemisphere tradewinds, off the coast of Kenya, and both flow offshore. As the NE monsoon relaxes, the EACC pushes farther northward, causing the coastal currents to reverse prior to the local wind reverses along the coast of Kenya and southern Somalia (Leetmaa, 1972; Anderson, 1981). By mid-April, the

southern Somalia (Leetmaa, 1972; Anderson, 1981). By mid-April, the

winds in the Southern Hemisphere reverse, turning first onshore and then northward, as the Southern Hemisphere tradewinds extend to the northwest. There is northward flow up to the equator, where it turns offshore and recirculates to the south forming a southern gyre. There is weak northward flow north of 5°N, with southward flow between the equator and 5°N. In May, the winds reverse all along the Somali coast. The winds are actually a jet-like structure (Findlater, 1971), fed in the south by the Southern Hemisphere tradewinds. This jet, known as the Findlater jet, is the atmospheric equivalent of an oceanic western boundary current, confined in the west by the highlands of Kenya and Ethiopia. Much of the jet's path is over land at very low latitudes. The Findlater jet migrates northward as it intensifies during the SW monsoon, so that the wind reversal occurs at different times at different latitudes. There is northward flow and upwelling all along the Somali coast, but the southern gyre still turns offshore within a few degrees north of the equator. In early June, the core of the Findlater jet crosses the coast at about 8°N and becomes very strong. At this time a second gyre appears between 4°N and 8°N. It was this gyre that was described by Findlay (1866) as the great whirl. By late June, the two gyre system is well established, with wedges of cold upwelled water extending out from the coast just to the north of the offshore flow in both gyres. This pattern remains quasi-stationary until late July or early August, when the winds

the north of the offshore flow in both gyres. This pattern remains quasi-stationary until late July or early August, when the winds

begin to weaken. At this time, the southern cold wedge migrates rapidly northward and merges with the northern wedge, signaling the coalescence of the two gyres. The Somali Current is now a more or less continuous boundary current from 10°S to 10°N. Sometime during the height of the SW monsoon, another clockwise gyre appears to the east of the island of Socotra, appropriately named the Socotra Eddy (Bruce, 1979). This eddy also appears to be a regular feature of the seasonal cycle. Sometime in October, the winds again reverse with the onset of the NW monsoon, and the southward Somali Current quickly develops. Much less is known about this part of the cycle, as it is much less dramatic and has not aroused as much attention.

The features described above have proven to be highly repeatable. The presence of the two gyre system was found in historical data for most of the years where there was sufficient data by Swallow and Fieux (1982). Bruce (1973, 1979) found the two gyre system in 1970 and 1976, and it also was quite prominent in the 1979 INDEX observations (Schott and Quadfasel, 1982; Leetmaa, et al., 1982; Swallow et al., 1983). Bruce (1979) also documented the presence of the Socotra Eddy in the four years from 1975-78. The observations indicate that the great whirl forms north of 4°N (Schott and Ouadfasel, 1982), rather than being advected from the equator as some theories suggest (eg. Hurlburt and Thompson, 1976; Cox, 1976, 1979; Lin and Hurlburt, 1981). It thus appears that different mechanisms are responsible for the development of the

Cox, 1976, 1979; Lin and Hurlburt, 1981). It thus appears that different mechanisms are responsible for the development of the

southern and northern gyres. Anderson (1981) implies that the southern gyre is forced by the Southern Hemisphere tradewinds, and the current crosses the equator due to inertial overshoot as in Anderson and Moore (1979), while the great whirl is generated farther to the north by the Finlater jet as it leaves the coast around 9°N. Lin and Hurlburt (1981) have also shown that the great whirl can be generated in this manner. Schott and Quadfasel (1982) suggest that the local curl of the wind stress in the developing Findlater jet may also be important in the generation of the great whirl.

Several authors have tackled the question of the relative importance of remote vs local forcing in the generation of the Somali Current system (see Knox and Anderson (1984) for a review). Most conclude that local forcing effects, i.e., those within the boundary region, are important for the early stages of the current spin-up, but that remote forcing effects become important at a later time. These models usually included a very idealized wind stress forcing, with the region of wind stress curl located far away from the boundary, and neglected the spatially and temporally very complicated structure of the wind field over the Indian Ocean. In Luther and O'Brien (1984) they used observed climatological winds in a model with a realistic geometry, and were able to reproduce most of the observed features described above. The presence of a large, time-varying region of wind stress curl within and just offshore of the observed features described above. The presence of a large, time-varying region of wind stress curl within and just offshore

of the boundary region was a key factor in the development of the Somali Current system in that model. The fact that the model included the entire seasonal cycle was also shown to be important in accurately simulating the observed circulation patterns.

In this paper we will use the model described in Luther and O'Brien (1984) driven by the monthly mean of the winds from the first GARP Global Experiment (FGGE) of 1979, and compare those results to those from the model driven by the monthly mean climatology (MMC) winds. We will concentrate on the development and decay of the two gyre system in these two cases. It will be shown that the great whirl develops at about 5°N under the influence of the local or very nearby wind stress curl, while the southern gyre responds to the local winds and the Southern Hemisphere tradewinds. The two gyre system collapses when the westerly component of the winds at the equator begin to decrease. Not only is the local wind stress curl important, but also the strong gradient in the wind stress curl associated with the Findlater jet greatly influences the development of the Somali Current system through a differential Ekman pumping.

We will briefly describe the model in the next section, and then compare and contrast the two different wind fields used to drive the model. We next will describe and compare the model results in the two cases before finally interpreting these results in the context of previous theoretical work.
results in the two cases before finally interpreting these results in the context of previous theoretical work.

THE MODEL

We use the nonlinear reduced gravity transport equations to model the upper ocean response to an applied wind stress. Due to the latitudinal extent of the model, we use spherical coordinates, with φ (longitude) increasing eastward and θ (latitude) increasing northward. If we define the eastward and northward components of the upper layer transport as $U = uH$ and $V = vH$ respectively, where (u, v) are the depth-independent (φ, θ) velocity components in the upper layer and H is the thickness of the upper layer, the equations of motion are

$$\frac{\partial U}{\partial t} + \frac{1}{a\cos\theta}\frac{\partial}{\partial\varphi}\left(\frac{U^2}{H}\right) + \frac{1}{a}\frac{\partial}{\partial\theta}\left(\frac{UV}{H}\right) - (2\Omega\sin\theta)V$$

$$= \frac{-g'}{2a\cos\theta}\frac{\partial H^2}{\partial\varphi} + \frac{\tau(\varphi)}{\rho_1} + A\nabla^2 U \qquad (1a)$$

$$\frac{\partial V}{\partial t} + \frac{1}{a\cos\theta}\frac{\partial}{\partial\varphi}\left(\frac{UV}{H}\right) + \frac{1}{a}\frac{\partial}{\partial\theta}\left(\frac{V^2}{H}\right) + (2\Omega\sin\theta)U$$

$$= \frac{-g'}{2a}\frac{\partial H^2}{\partial\theta} + \frac{\tau(\theta)}{\rho_1} + A\nabla^2 V \qquad (1b)$$

$$\frac{\partial H}{\partial t} + \frac{1}{a\cos\theta}\left(\frac{\partial U}{\partial\varphi} + \frac{\partial}{\partial\theta}(V\cos\theta)\right) = 0 \qquad (1c)$$

6

where $g' = \frac{(\rho_2-\rho_1)}{\rho_2} g$ is the reduced gravitational acceleration, a is the earth's radius, Ω is the earth's rotation rate, and A is a kinematic eddy viscosity. The wind stress, $\vec{\tau} = (\tau(\phi), \tau(\theta))$, is applied as a body force over the upper layer (Charney, 1955). The transport form of the reduced gravity equations has the advantage that the continuity equation (1c) is linear. It also has the advantage that the discretization of the advective terms in (1a) and (1b) involves spatial averaging of the dependent variables, thus improving the numerical stability of the solution.

For the model geometry, we simulate the coastline of the Arabian Sea from 40E to 73E and from 10S to 25N. The model geometry is shown in Fig. 1. The boundary conditions along all solid (land) boundaries are the no slip conditions:

$$u = v = 0$$

The southern boundary along 10S and a portion of the eastern boundary, from 5S to the equator, are open boundaries, the boundary condition there being a variation of the Sommerfeld radiation condition developed by Hurlburt (1974) and described in Camerlengo and O'Brien (1980). The eastern boundary from the equator to the Gulf of Khambat is closed, and the no slip boundary condition applies there. This simulates the Laccadive and Maldive islands

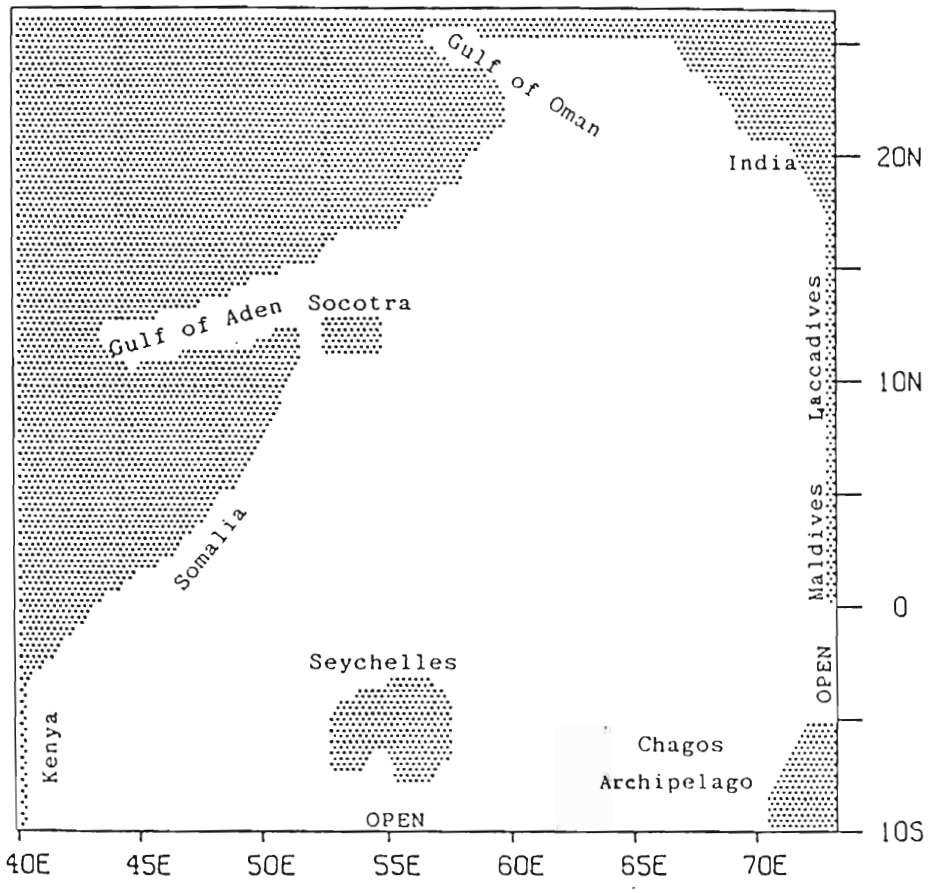

Fig. 1.

Model Geometry. Shading indicates land boundaries. The islands of Socotra and the Seychelles and their surrounding shallow banks are represented as land boundaries. The southern boundary and a portion of the eastern boundary are open.

Model Geometry. Shading indicates land boundaries. The islands of Socotra and the Seychelles and their surrounding shallow banks are represented as land boundaries. The southern boundary and a portion of the eastern boundary are open.

which close off the eastern side of the Arabian Sea. The south-eastern corner of the model basin is closed off by the Chagos Archipelago, and again, the no slip boundary condition applies along the coast of this island.

Eqs. (1) are solved numerically on a 135 x 74 finite difference mesh. The solution mesh is staggered in space as shown in Fig. 2. The model resolution is 1/8° in the zonal direction ($\Delta\phi$) and 1/4° in the meridional direction ($\Delta\theta$). The equations of motion are integrated in time using a leapfrog finite difference scheme, with a forward time difference used every 99th time step to eliminate the computational mode. The model time step is 30 min. The advective terms are computed by first averaging adjacent U, V and H values in space to form the desired product at the appropriate meshpoint and then forming the standard, second order accurate, centered finite difference approximation. The spatial averaging helps suppress nonlinear growth of numerical noise in the model.

In the linearized form of the reduced gravity equations, one must prescribe the linear phase speed for the particular baroclinic mode one wishes to model: $C^2 = g'H_o$. In the nonlinear form, there is no analogous phase speed parameter, only g'; however, in the numerical solution of (1) one must prescribe the initial upper layer thickness, H_o. This is analogous to prescribing an initial phase speed, but this does not remain constant as the model fields evolve,

speed, but this does not remain constant as the model fields evolve,

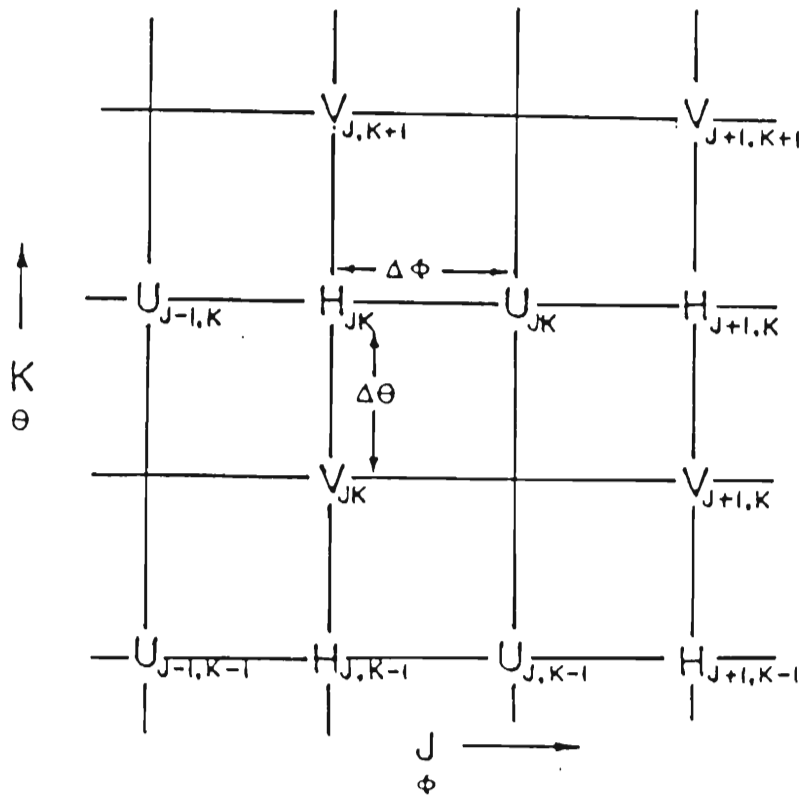

Fig. 2.

Staggered mesh used in finite difference approximation, showing relative location of U, V and H points. J is the index in the zonal (ϕ) direction and K is the meridional (Θ) index.

as the variations in H are large compared to H_o. The average thickness of the upper layer is not constant, due to inflow and outflow at the open boundaries during the seasonal cycle. The other free parameter in the model is the kinematic eddy viscosity, A. This frictional term is required to damp out the grid scale noise in the model to prevent this noise from growing through nonlinear interactions.

For the results presented here, we set H_o = 300 m, $A = 1.4 \times 10^3$ $m^2 s^{-1}$ and the reduced gravity $g' = 0.03$ m s^{-2}. The model is integrated from rest, beginning at 0000 GMT on 1 January, using an exponential taper with an e-folding time of 20 days to reduce the initial transients. For simplicity, the model year has 360 days, with each month having 30 days.

THE WIND FORCING

Two different wind data sets are used to derive the forcing fields for the model. For one case, we use the dynamically assimilated FGGE Level III-b wind data (see Bengtsson et al. (1982)), obtained from the National Center for Atmospheric Research. These data consist of global analyses on a 1.875° latitude by 1.875° longitude mesh at each of 15 standard levels every 12 hours (every 6 hours during the winter and summer special observing periods) from 00h GMT on 1 December 1978 to 12h GMT on 30 November 1979. We extract the winds only at the 1000 mbar level, and form a psuedostress from each observation. The psuedostress is defined as the wind vector $\vec{W}$ multiplied by its magnitude: $\vec{W}|\vec{W}|$. We then compute the monthly mean psuedostress from these data to facilitate comparison with the MMC data.

The MMC data were obtained from the United States National Climate Center in Ashville, North Carolina, from their Global Marine Sums TD-9757 data set. These data consist of standard meteorological observations compiled on 1° Marsden squares from over 60 years of ship reports. This data set was derived from the TD-11 data, that were also used by Hastenrath and Lamb (1979). The wind observations consist of an averaged 8-point wind rose on each 1° square for each month of the year. From this wind rose, we compute a psuedostress

vector for each of the eight compass directions, and then average these vectors to get the monthly mean psuedostress on each square. The data are smoothed by a Hanning filter in both directions, additionally weighted by the number of observations on each square. The resultant fields compare well to those computed by Bruce (1983) and by Hellerman and Rosenstein (1983) for this area.

Once we have a monthly mean psuedostress for both wind data sets, they are treated identically, allowing, of course, for the different spatial resolutions. To interpolate from the monthly mean to the model time step, we compute the mean and first five Fourier harmonics at each point, and use these to construct daily values for the year. We then interpolate linearly from the daily values to the model time step. To interpolate in space from the wind data mesh to the model mesh, we use the natural bicubic spline interpolant. This results in a complete annual cycle of wind psuedostress for both the FGGE and MMC cases that is continuous in space and time and has continuous first and second derivatives in space. These psuedostress fields are converted to wind stress by the bulk aerodynamic formula:

$$\vec{\tau} = \rho_a C_D \vec{W} |\vec{W}| \qquad (2)$$

where ρ_a is the density of air and C_D is a constant drag coefficient. For the results presented here, we use the values ρ_a = 1.2 kg m^{-3} and $C_D = 3.75 \times 10^{-3}$. The large value for C_D is used because we are projecting the wind stress on such a deep upper

1.2 kg m^{-3} and $C_D = 3.75 \times 10^{-3}$. The large value for C_D is used because we are projecting the wind stress on such a deep upper

layer. As we will show, the upper layer transports driven by the wind stress values thus obtained agree well with observations.

As stated above, we will concentrate here on the period March to October, which includes the SW monsoon and both transitions. Figure 3 shows the model wind stress for March from the FGGE case. This is the transition period from the NE monsoon to SW monsoon conditions. The wind stress from the MMC case at this time are very similar. The Northern Hemisphere winds are still dominated by the NE monsoon, while the Southern Hemisphere winds are beginning to break up, and have an onshore component along the coast at 5°S. There is a convergence zone at 8-10°S, from 50°E to 70°E. In early April in the FGGE case, the winds along the southern Somalia and Kenya coasts reverse as the Southern Hemisphere tradewinds extend toward the northwest (Fig. 4). The convergence zone is now at about 7°S. The winds in the Northern Hemisphere have turned to onshore along the Somali coast. The northern Arabian Sea is dominated by a weak anticyclonic circulation, with stronger winds to the east along the Indian coast. The equatorial winds are easterly in the western part of the basin, and westerly in the eastern part. The patterns are somewhat similar in the MMC case (Fig. 5). The strength of the Southern Hemisphere tradewind extension is not as great. Westerly winds cover much more of the equatorial region in this case, and the convergence zone is slightly farther to the north. The winds along the Indian coast are also much weaker.

convergence zone is slightly farther to the north. The winds along the Indian coast are also much weaker.

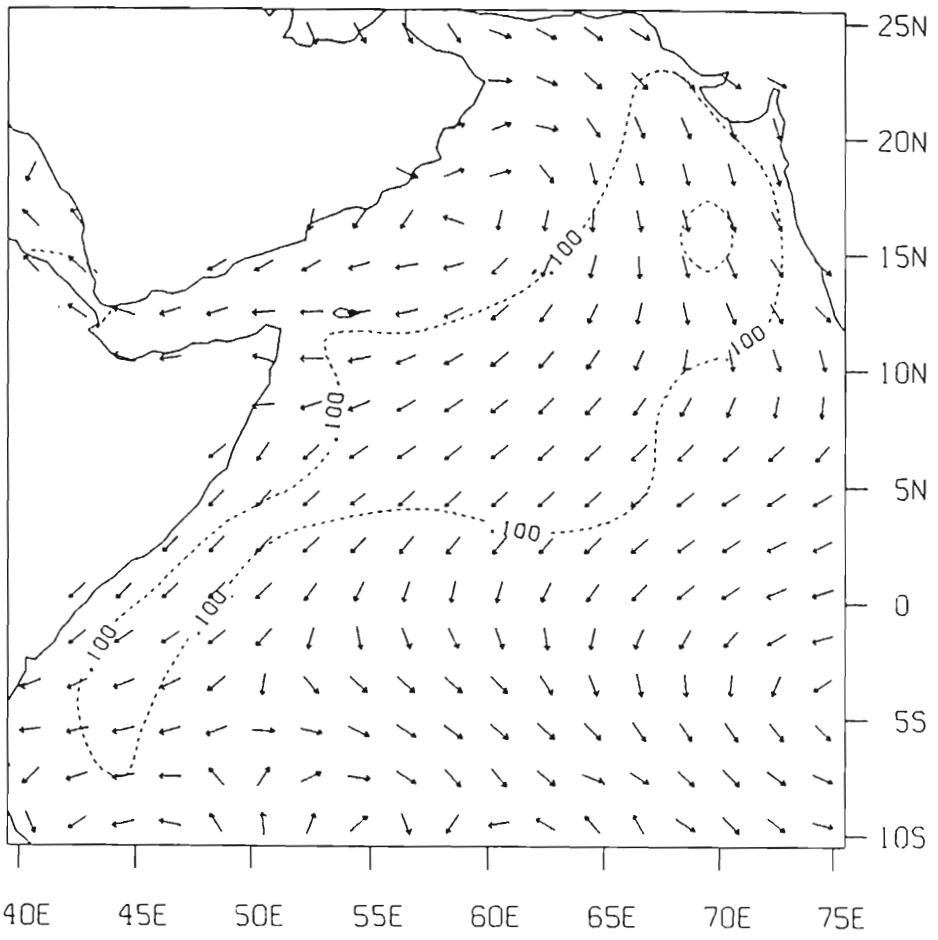

Fig. 3.

Model wind stress derived from the FGGE wind data for 16 March. Arrows indicate direction, while contours give magnitude. The winds are weak and variable, but with some southwestward wind stress remaining from the NE monsoon. Contour interval is 0.1 N m^{-2}.

remaining from the NE monsoon. Contour interval is 0.1 N m^{-2}.

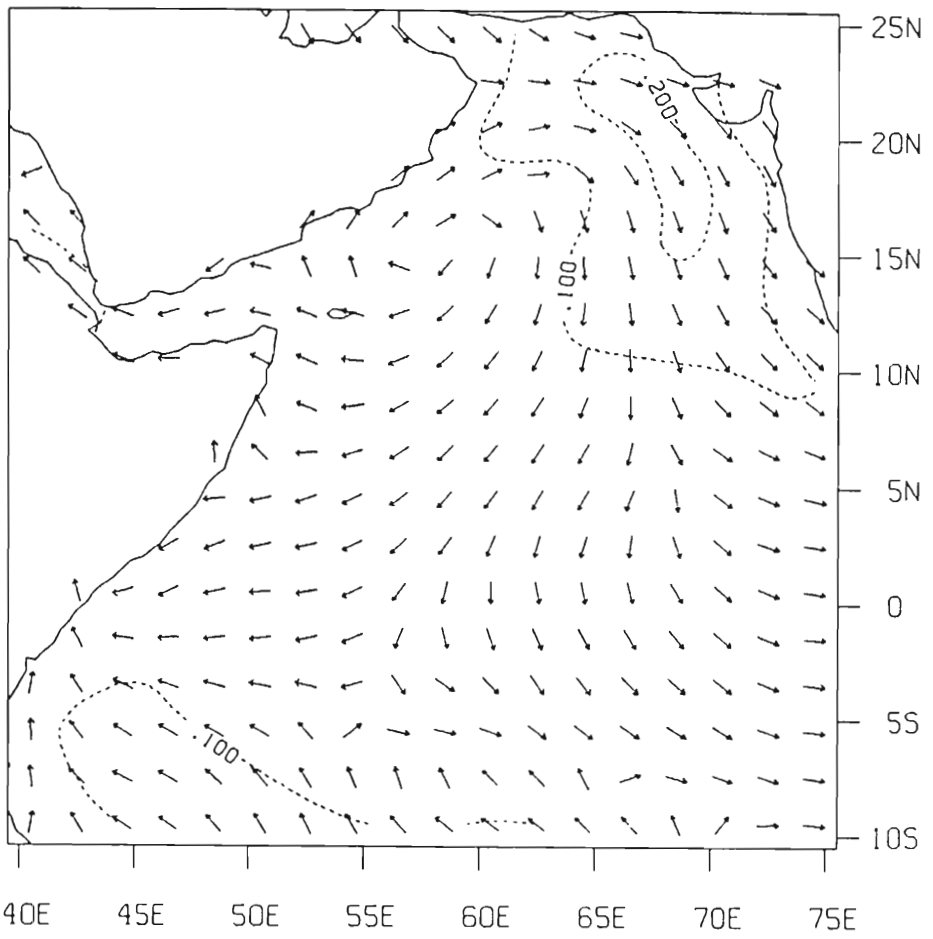

Fig. 4.

Model wind stress derived from the FGGE wind data for 16 April. The winds along the southern Somali coast reverse in early April, due to a westward extension of the Southern Hemisphere tradewinds, while north of the equator the winds are still light and variable.

north of the equator the winds are still light and variable.

Contour interval is 0.1 N m^{-2}.

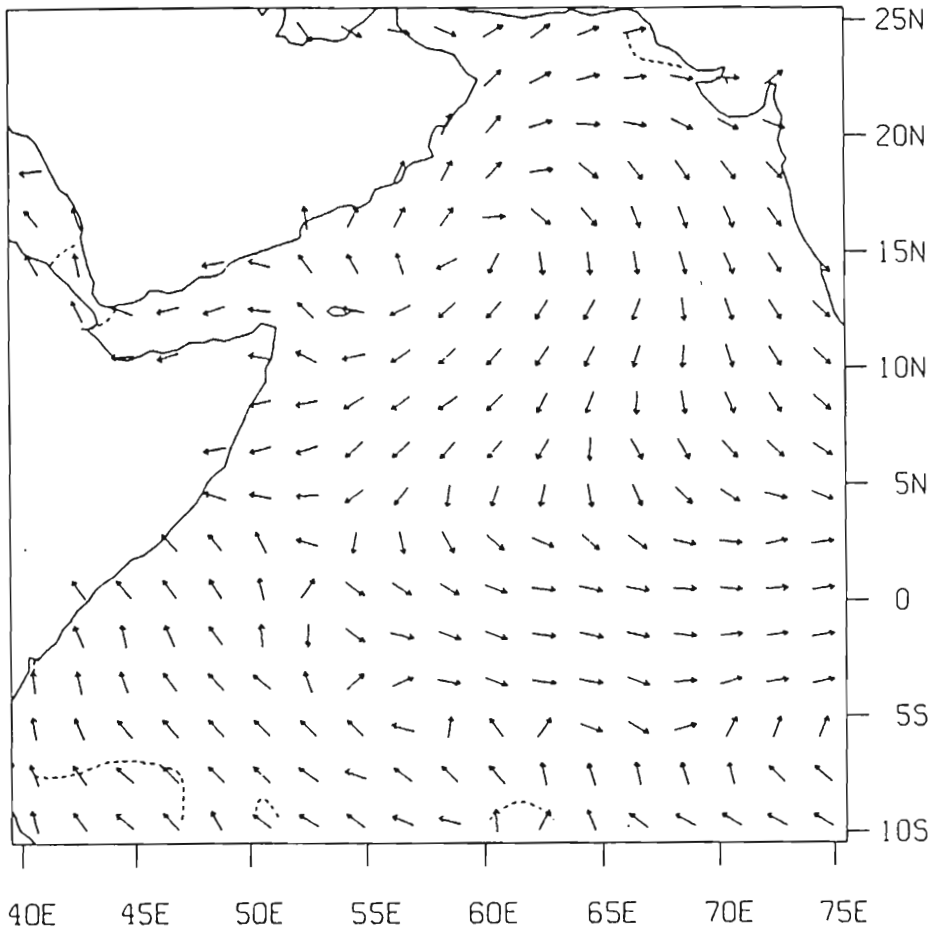

Fig. 5.

Model wind stress derived from the MMC case for 16 April. Winds are very light, with some weak northward winds beginning to form along the Somali coast south of the equator. The westward extension of the Southern Hemisphere trades is not as strong in this case, possibly because of the sparse number of observations along 10°S.
the Southern Hemisphere trades is not as strong in this case, possibly because of the sparse number of observations along 10°S.
Contour interval is 0.1 N m^{-2}.

In May (Fig. 6 and 7) the winds become south-southwesterly all along the coast of Somalia and Kenya. The Findlater jet can now be seen in both cases, although it is more intense in the FGGE case. The Southern Hemisphere tradewinds have penetrated much farther north in the FGGE case, and consequently the convergence zone is farther north. The jet pushes farther inland over Kenya and Somalia near the equator in the FGGE case, resulting in a minimum in the alongshore wind stress at the equator. In the FGGE case, the jet is strongest in the Southern Hemisphere trades, and in the extreme northern Arabian sea, while in the MMC case the strongest winds occur off the northern Somali coast. Westerly winds are found along the equator east of 58°E in both cases.

The wind stress curl distribution is very different in the two cases, as can be seen from Fig. 8 and 9. Most of the differences can be attributed to differences in the strength and location of the Findlater jet. Since the jet is more intense in the FGGE case, the horizontal shears are larger and the curl is therefore greater. Much of this can be attributed in turn to the effect of the climatological averaging -- the interannual variability in the position of the jet tends to make it more diffuse in the mean. The curl field in the FGGE case is of course much smoother, because the data were dynamically assimilated using a global general circulation model (Bengtsson et al., 1982), which tends to produce relatively smooth curl fields. The gross features, however, are similar in some

model (Bengtsson et al., 1982), which tends to produce relatively smooth curl fields. The gross features, however, are similar in some

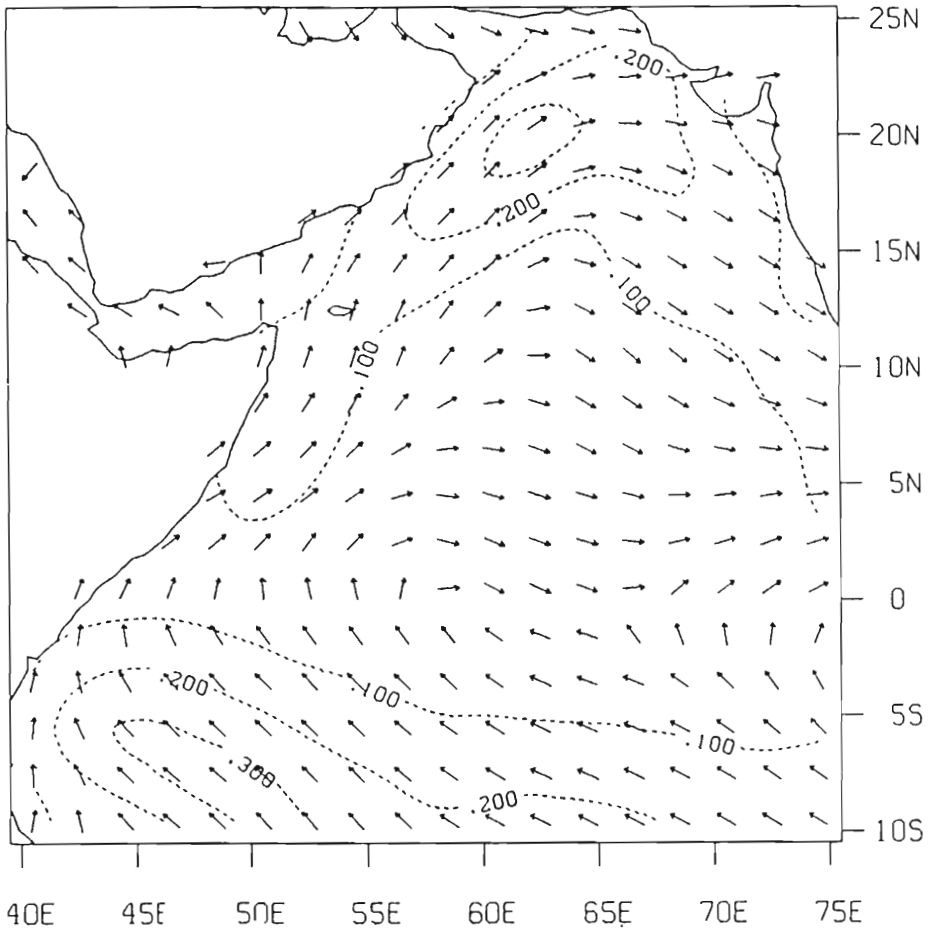

Fig. 6.

Model wind stress from the FGGE case for 16 May. Northeastward winds are now found all along the coasts of Africa and Arabia. The maximum wind stress occurs in the Southern Hemisphere as a northwestward extension of the tradewinds. Simultaneously, another area of large wind stress builds over the northern Arabian Sea, forming the beginnings of the Findlater jet. There is a belt of weak convergent winds along the equator. Contour interval is 0.1 N m^{-2}.

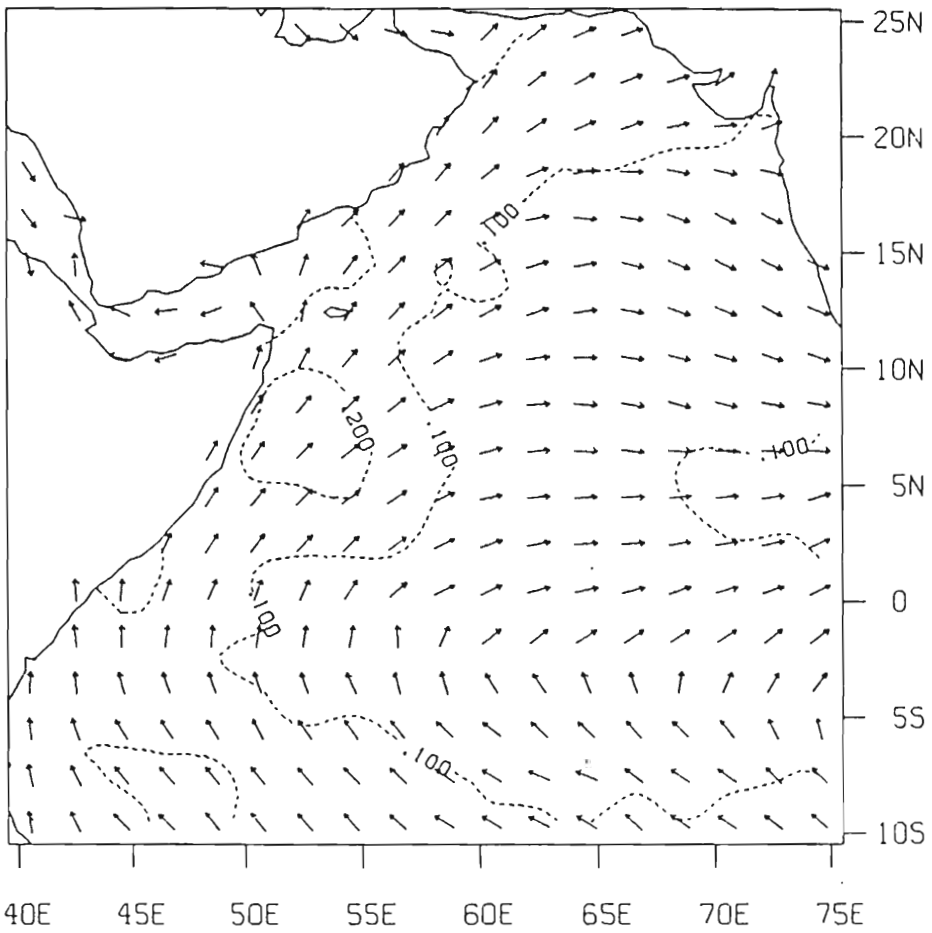

Fig. 7.

Model wind stress from the MMC case for 16 May. North to northeastward winds are also found along the African and Arabian coasts, although not as strong as in the FGGE case, particularly in the Southern Hemisphere tradewind extension and in the extreme
coasts, although not as strong as in the FGGE case, particularly in the Southern Hemisphere tradewind extension and in the extreme
northern Arabian Sea. Contour interval is 0.1 N m^{-2}.

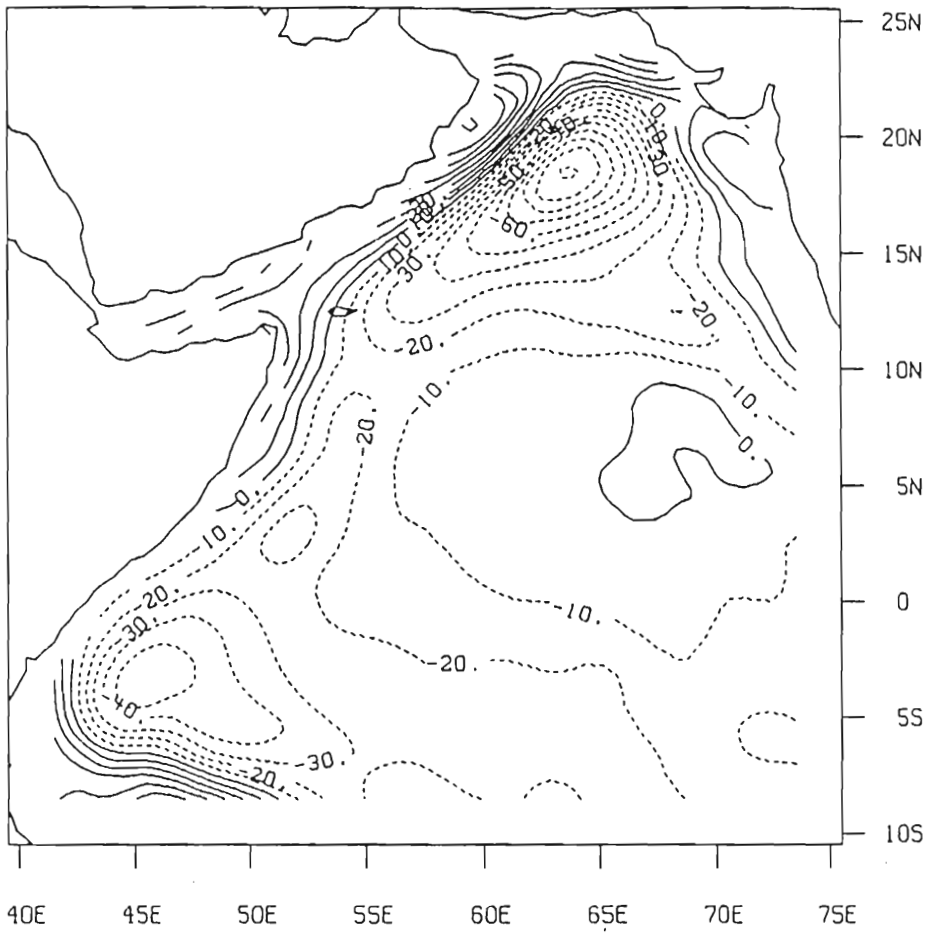

Fig. 8.

Wind stress curl from the FGGE case for 16 May. Dashed contours indicate negative values. A large patch of negative curl has developed over the northern Arabian Sea, associated with the developing Findlater jet. Another less intense area of negative curl has formed off the southern Somali coast, associated with the extension of the Southern Hemisphere trades. From the equator to 10°N, there is almost no curl to the wind stress. Contour interval is 1.0×10^{-7} N m^{-3}. Labels are in units of 10^{-8} N m^{-3}.

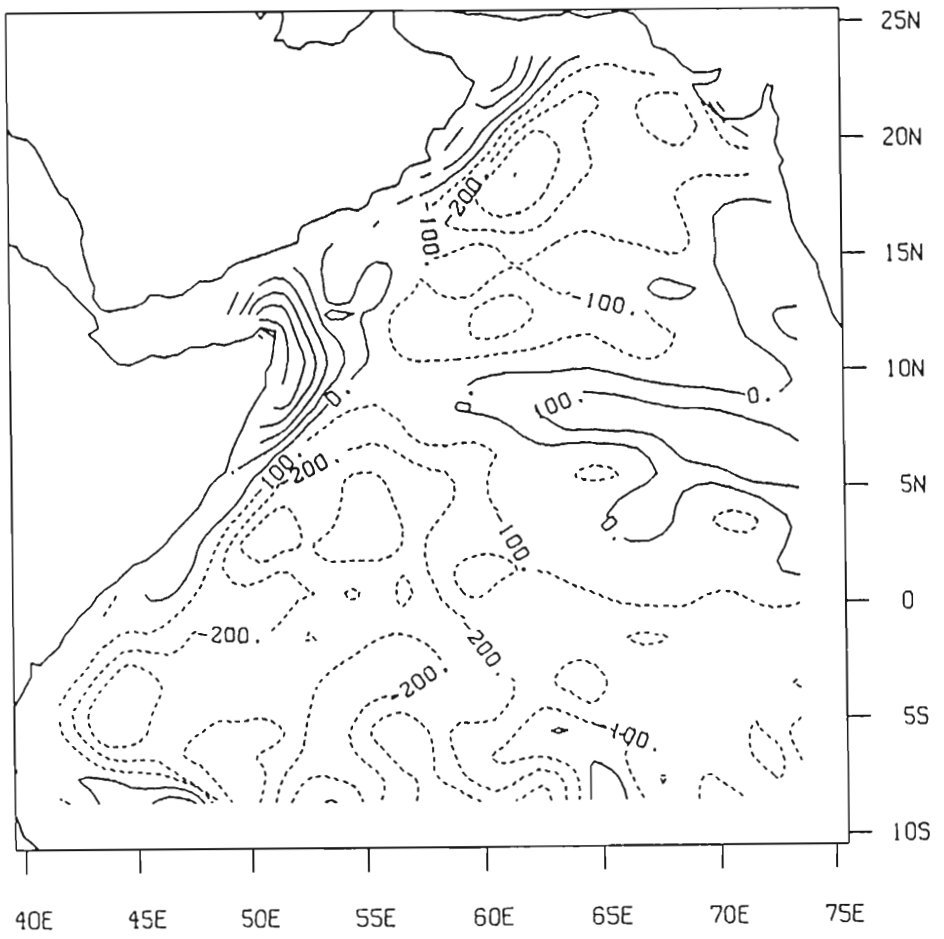

Fig. 9.

Wind stress curl from the MMC case for 16 May. The patch of negative curl over the northern Arabian Sea is much weaker than in the FGGE case, because the Findlater jet is not as well developed at this time in this case. The negative curl in the Southern Hemisphere is almost as strong as in the FGGE case, even though the winds are much weaker. This is due to the northeastward turn the winds must make as they approach the African continent. Contour interval is 1.0×10^{-7} N m^{-3}. Labels are in units of 10^{-9} N m^{-3}.

respects. There are large areas of negative curl to the right of the core of the jet (facing downstream), and a line of zero curl that roughly follows the core of the jet. The areas of negative curl are found off the southern Somali coast where the southern hemisphere tradewinds turn northward to feed the jet, and over the northern Arabian Sea, where the jet is most intense, and where it bends eastward toward the Indian subcontinent.

In early to mid-June (Fig. 10 and 11) the "main onset" of the SW monsoon occurs, and the strength of the wind increases dramatically. Maximum wind stress values are found just off the coast of northern Somalia where the Findlater jet leaves the coast. In the MMC case there are two relative maxima, one to the east and one to the south of Socotra, while in the FGGE case there is only one to the south of Socotra. Again the jet is more intense in the FGGE case for the reasons mentioned above. The convergence zone is found at about 2°N in the FGGE case and at about 2°S in the MMC case, resulting in easterly winds along the equator east of 62°E in the FGGE case, while the MMC winds are still westerly there. A large area of negative wind stress curl develops between the equator and 12°N, with maximum negative values occuring at 5°N in both cases (Fig. 12 and 13). In the MMC case, there is another relative maximum, stronger than the one at 5°N, located along 12°N. In both cases there is a very strong gradient in the wind stress curl that follows the core of the jet.

gradient in the wind stress curl that follows the core of the jet.

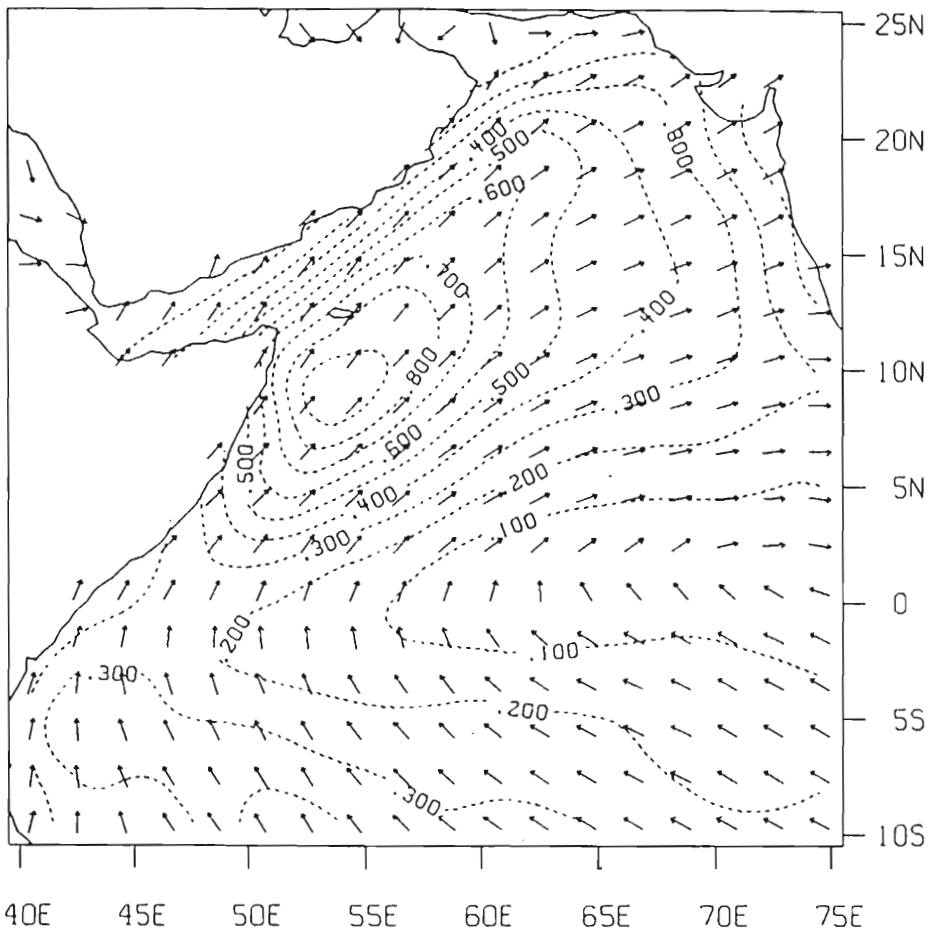

Fig. 10.

Wind stress from the FGGE case for 16 June. The area of maximum wind stress is now south of the island of Socotra, and the magnitude of the stress has increased dramatically. There is still a relative minimum in the stress along the equator, and the extension of the Southern Hemisphere trades has strengthened. Contour interval is 0.1 N m^{-2}.

Southern Hemisphere trades has strengthened. Contour interval is 0.1 N m^{-2}.

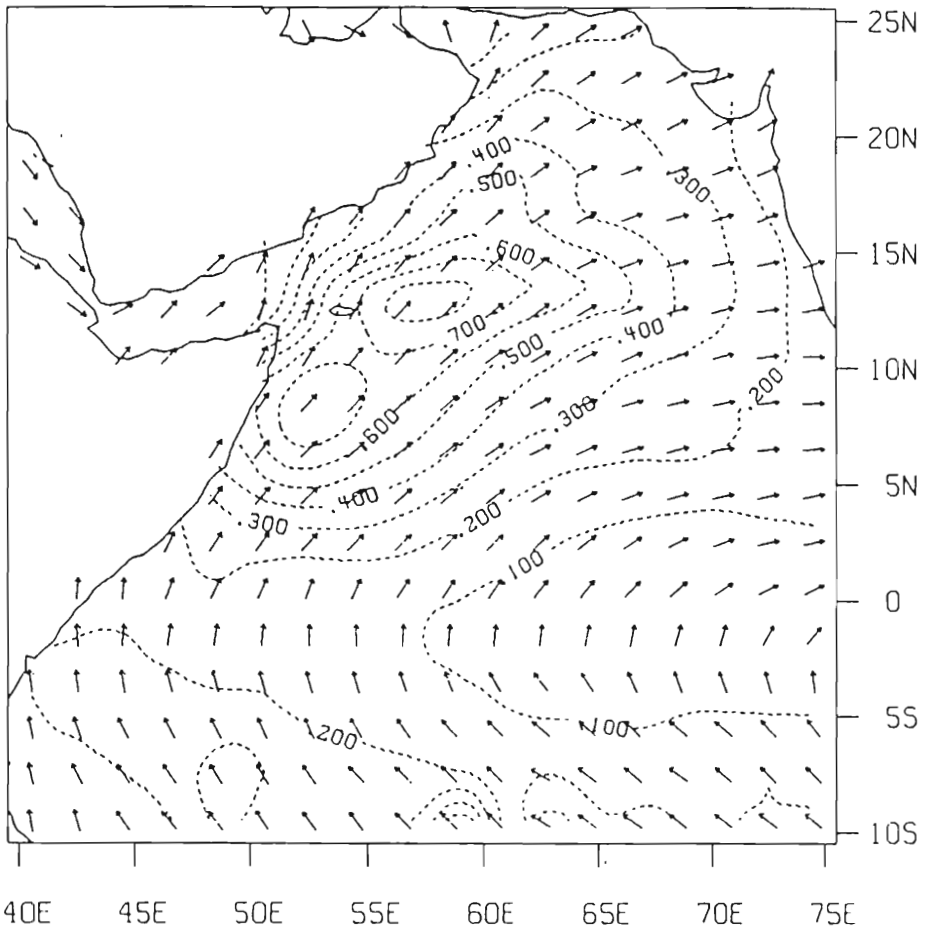

Fig. 11.

Wind stress from the MMC case for 16 June. There are two relative maxima in the Northern Hemisphere, one to the east of Socotra, and another to the south. The minimum stress is again found along the equator, and the extension of the Southern Hemisphere trades has strengthened. Contour interval is 0.1 N m^{-2}.

strengthened. Contour interval is 0.1 N m^{-2}.

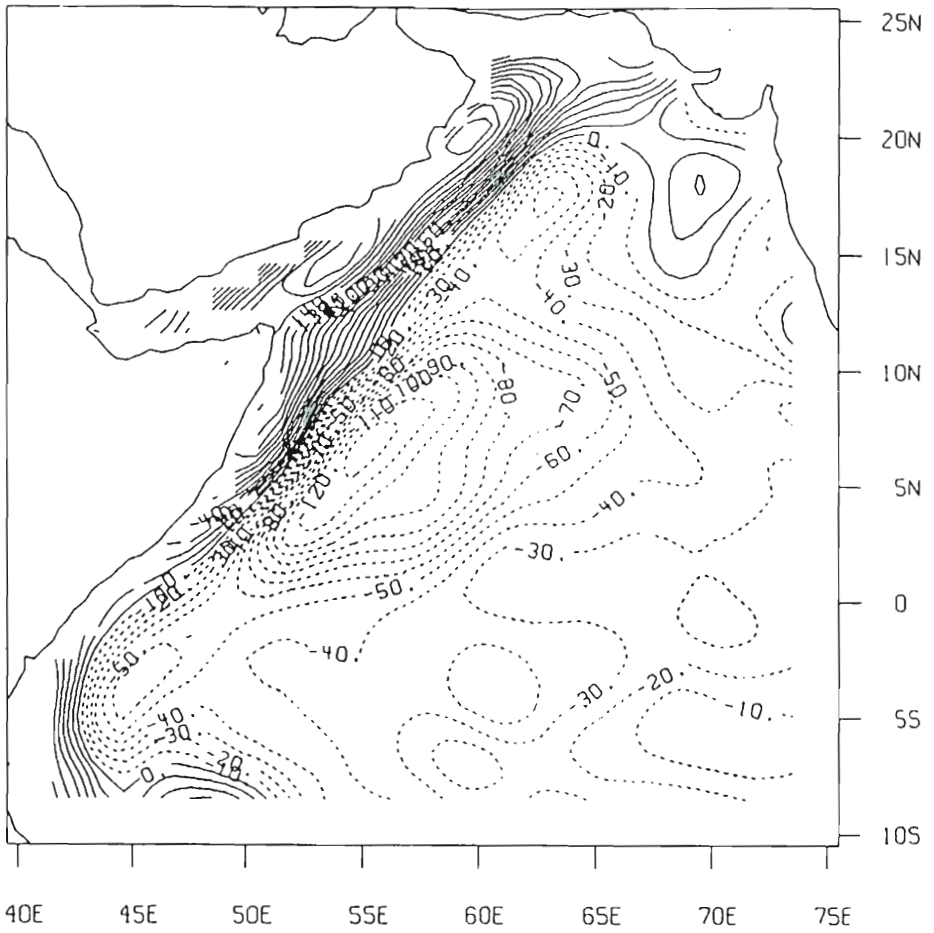

Fig. 12.

Wind stress curl from the FGGE case for 16 June. There are now three relative maxima in negative curl, with the most intense patch of negative curl centered at 5°N, 53°E, just off the Somali coast. There is a strong gradient of wind stress curl that roughly follows the core of the Findlater jet. This curl gradient causes a differential Ekman pumping, with downward Ekman pumping on the eastern side of the jet core, and upward Ekman pumping on the western side. This differential Ekman pumping can greatly influence
eastern side of the jet core, and upward Ekman pumping on the western side. This differential Ekman pumping can greatly influence the wind driven ocean circulation. Contour interval is 1.0×10^{-7} N m^{-3}. Labels are in units of 10^{-8} N m^{-3}.

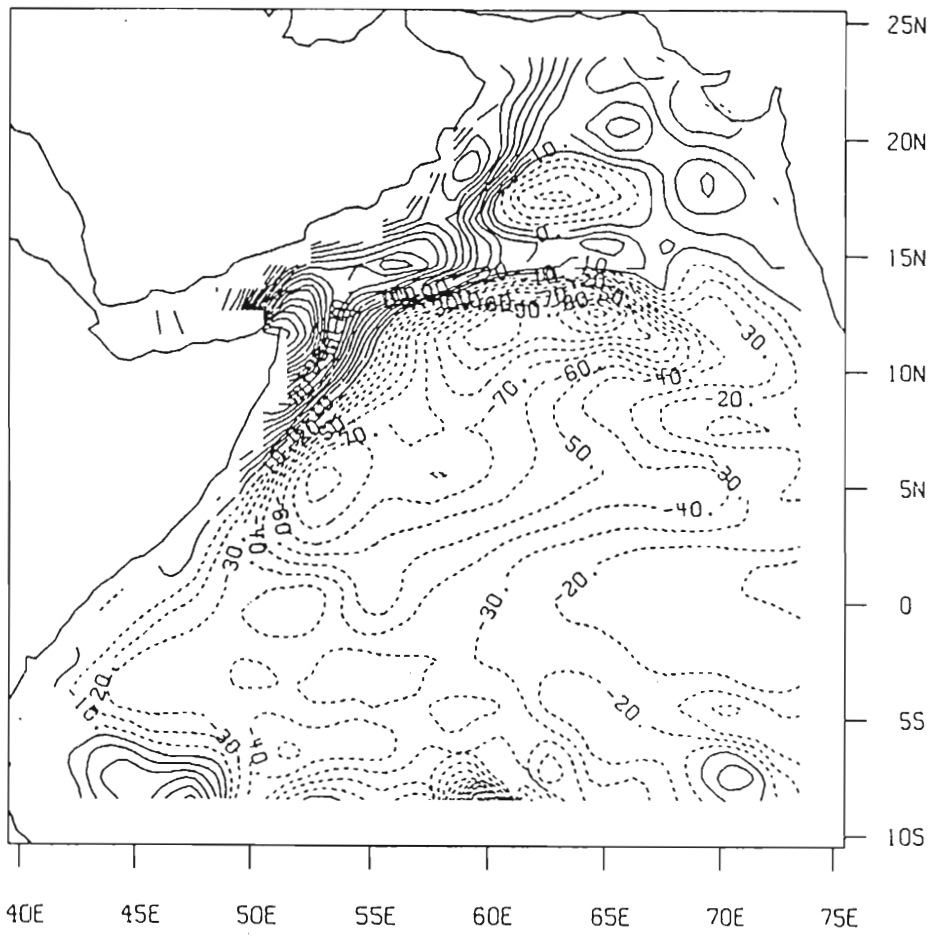

Fig. 13.

Wind stress curl from the MMC case for 16 June. The curl pattern is quite different from the FGGE case, but we still see a relative maximum in negative curl centerd at 5°N, 53°E. There is another relative maximum in negative curl to the east of Socotra, at about 12°N. There is also a strong gradient in the wind stress curl, but this gradient divides into two branches at 13°N. One branch is oriented east-west along 13°N, and the other, weaker branch trends

this gradient divides into two branches at 13°N. One branch is oriented east-west along 13°N, and the other, weaker branch trends

northeast-southwest, roughly paralleling the Arabian coast. Contour interval is 1.0×10^{-7} N m^{-3}. Labels are in units of 10^{-8} N m^{-3}.

In the MMC case (Fig. 13) this gradient splits at 13°N, with one branch oriented to the northeast and the other to the east along 13°N. This is an indication that the jet itself splits, as reported by Findlater (1971). One would expect that these strong gradients in the wind stress curl will greatly influence the ocean's response, since it will drive a corresponding gradient or differential Ekman pumping, i.e., upward Ekman pumping beneath the positive curl and downward pumping beneath the negative curl, resulting in a tilting of the pycnocline. We can see from Fig. 12 and 13 that the curl and its gradients are stronger in the FGGE case.

The height of the monsoon occurs in mid-July in both cases (Fig. 14 and 15). In the FGGE case, the maximum stress occurs southeast of Socotra, while in the MMC case, a single maximum now occurs to the east of Socotra. The maximum stress in the MMC case is about 20% lower than the FGGE case. In the FGGE case, the convergence zone is at 3°N, while in the MMC case it is still just south of the equator. The curl patterns for both cases (Fig. 16 and 17) are similar to those the preceeding month, but the curl and its gradients have become much stronger. Negative curl covers almost the entire basin, with the exception of the Arabian coastal region. The maximum negative curl is about the same in both cases, but occurs in different locations. Both cases have relative negative maxima in the curl at 7°-8°N, but in the MMC case the largest value of negative curl occurs along 13°N. It is important to note that in

maxima in the curl at 7°-8°N, but in the MMC case the largest value of negative curl occurs along 13°N. It is important to note that in

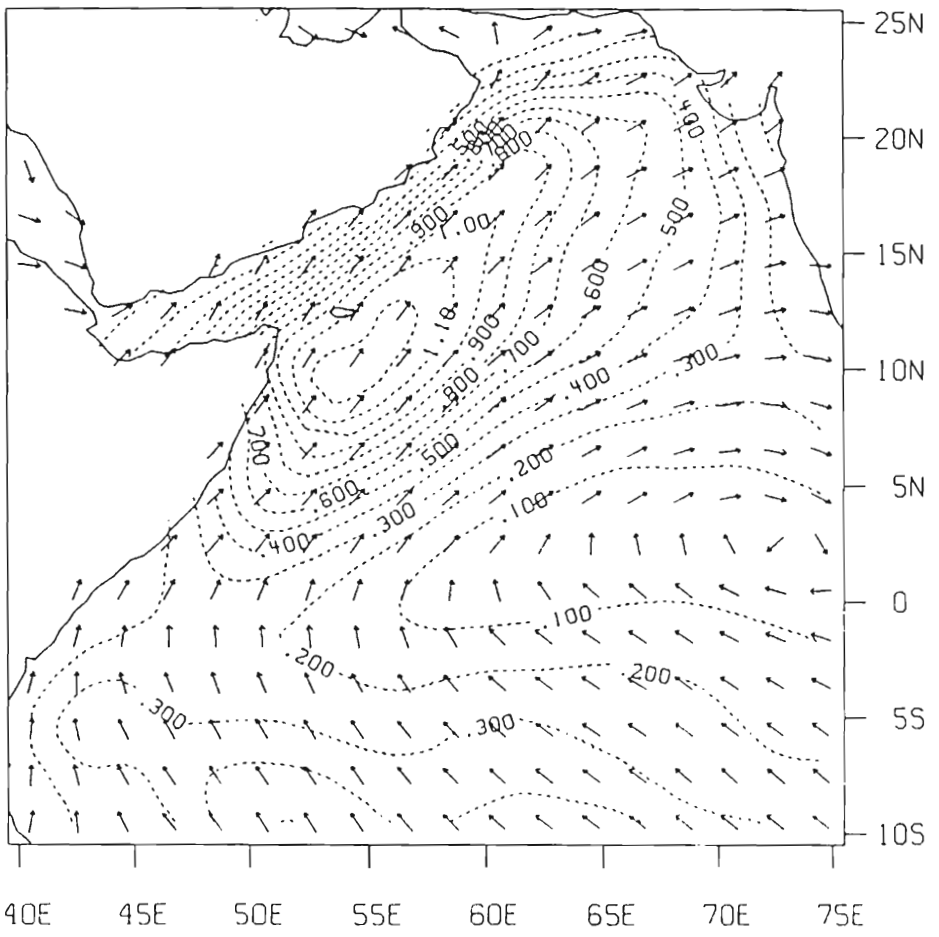

Fig. 14.

Wind stress from the FGGE case for 16 July. The winds reach their maximum intensity in mid to late July. The strongest winds occur to the south and east of Socotra, and the weakest winds occur along the equator. Contour interval is 0.1 N m^{-2}.

the south and east of Socotra, and the weakest winds occur along the equator. Contour interval is 0.1 N m^{-2}.

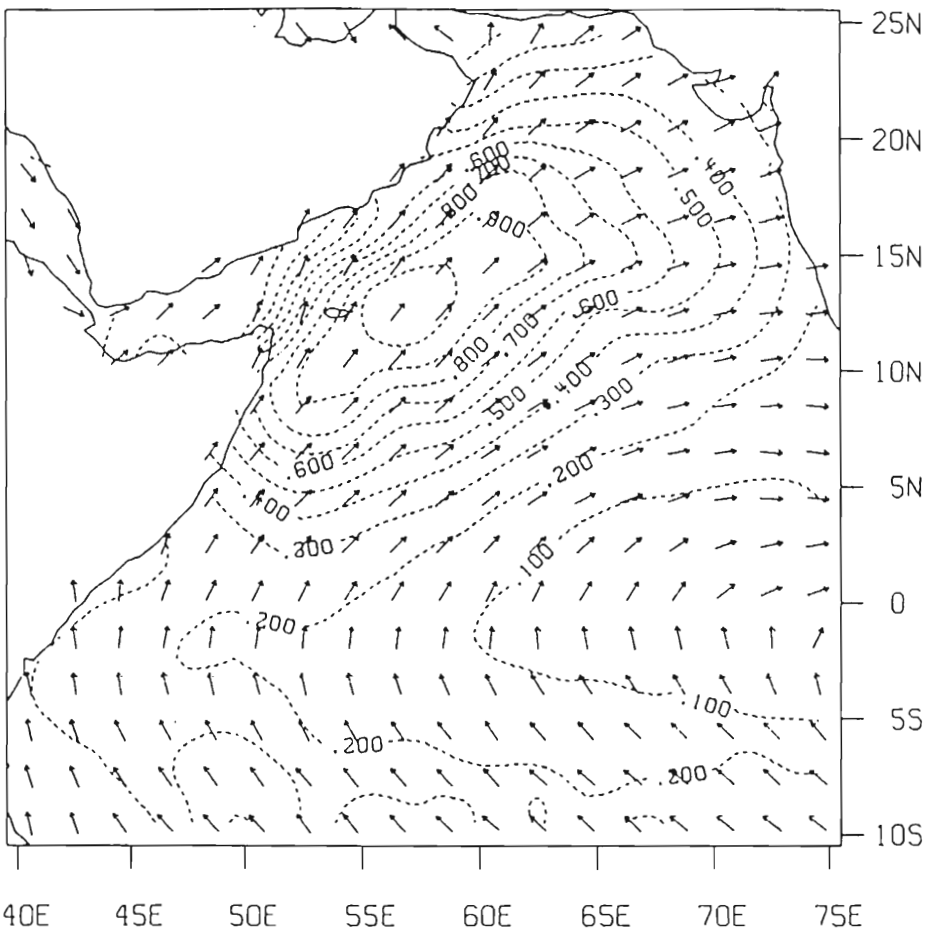

Fig. 15.

Wind stress from the NMC case for 16 July. The strongest winds occur in mid to late July in this case also, because of the Fourier harmonics interpolation scheme that was used in both cases. The pattern of the wind stress for this case is very similar to that for the FGGE case at this time, but the peak magnitude is about 20% lower. This is due to the effects of long term averaging and interannual variability. Contour interval is 0.1 N m^{-2}.

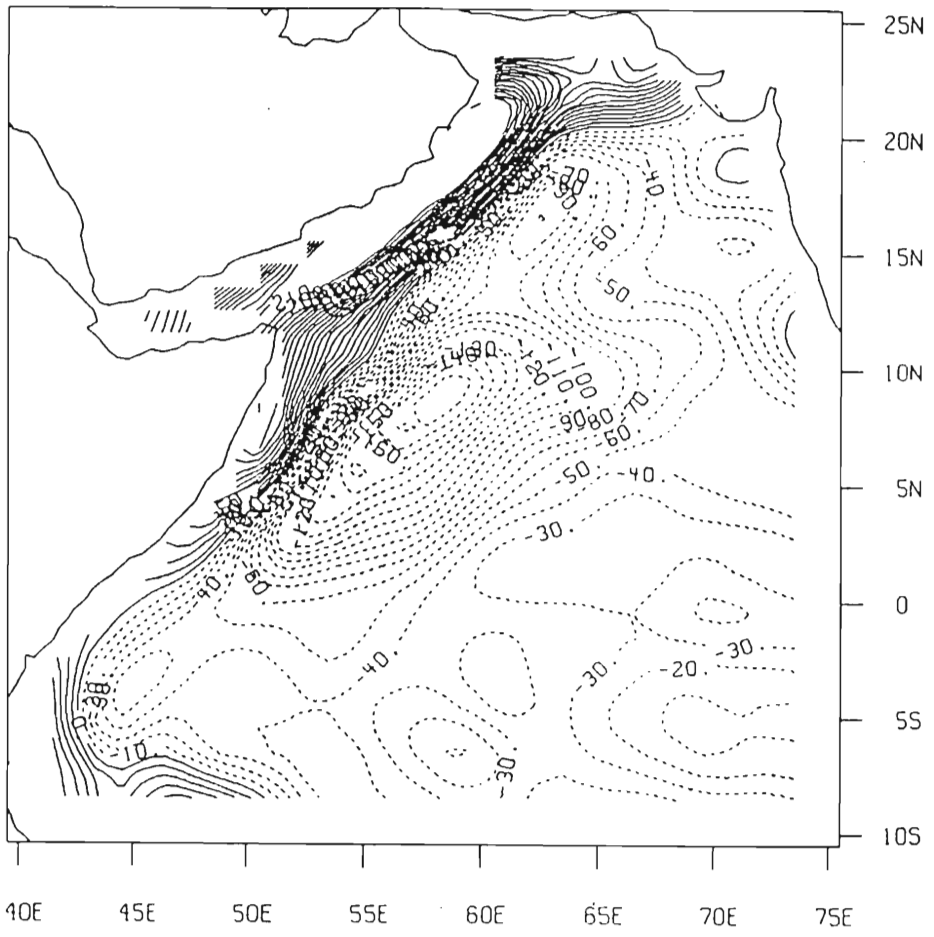

Fig. 16.

Wind stress curl from the FGGE case for 16 July. A very large patch of negative wind stress curl has formed off the Somali coast from south of the equator to 20°N, with the maximum negative values occurring, at 8°N, 58°E. The gradient of wind stress curl has intensified, but is in the same position as in the preceeding month. Contour interval is 1.0×10^{-7} N m^{-3}. Labels are in units of
intensified, but is in the same position as in the preceeding month. Contour interval is 1.0×10^{-7} N m^{-3}. Labels are in units of
10^{-8} N m^{-3}.

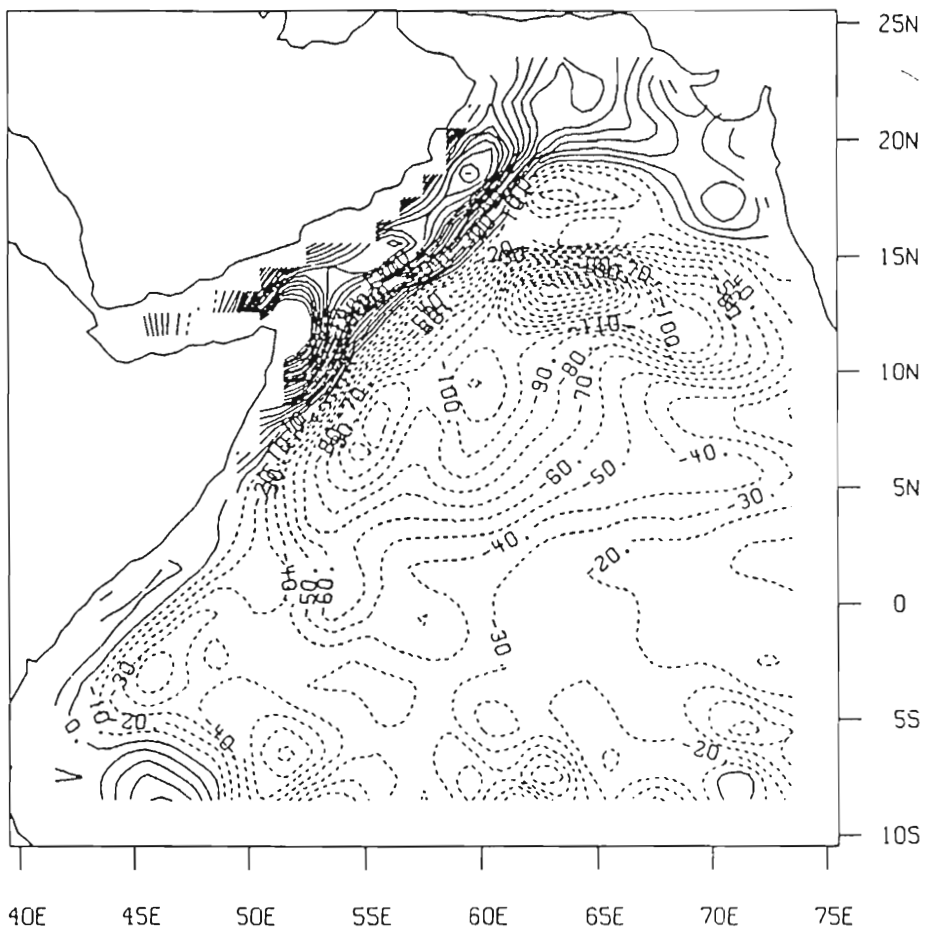

Fig. 17.

Wind stress curl from the MMC case for 16 July. There is strong negative curl offshore of the Somali and Arabian coasts, with maximum negative values occurring at 13°N, 63°E, and secondary relative maxima occurring at 6°N, 55°E and at 9°N, 59°E. The gradient of the curl, with its two branches, has intensified, but remains in approximately the same location. The maximum negative values of the curl are the same for this case as for the FGGE case, although their locations differ. Contour interval is 1.0×10^{-7} N m^{-3}. Labels are in units of 10^{-8} N m^{-3}.

both cases there are very large values of negative curl very near the Somali coast boundary region.

In mid- to late July the winds begin to relax. This relaxation is very rapid in August and September. The patterns in the stress and its curl remain much the same as those for July in both cases, but their magnitudes decrease substantially. By mid-September, (Fig. 18) the wind stress values are about 30% of their July values in both cases. The Southern Hemisphere tradewinds are retreating to the south. By late October, the Northern Hemisphere winds begin to reverse, and in mid-to late November, the northeasterly winds push across the equator, along the southern Somali and Kenya coasts. The NE monsoon is fully developed by late December.

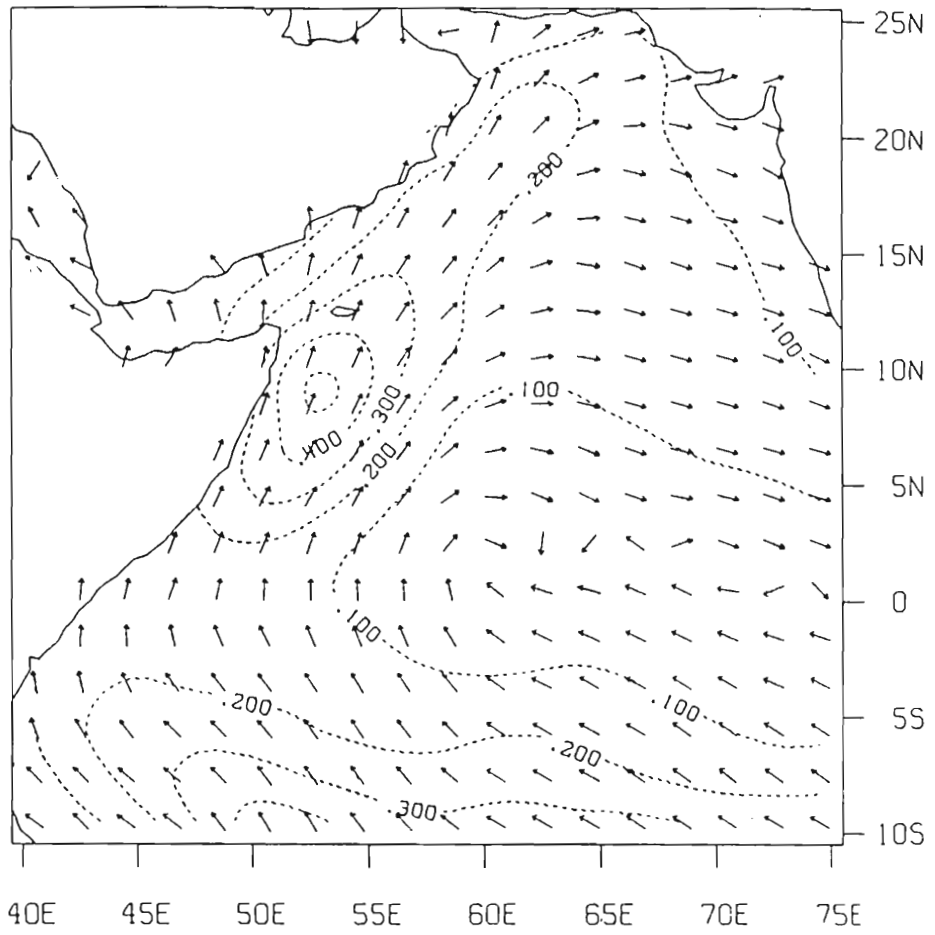

Fig. 18.

Wind stress from the FGGE case for 16 September. Beginning in late July and continuing through August and early September, both the wind stress and wind stress curl decrease in magnitude very rapidly in the FGGE and in the MMC cases. By mid-September, the maximum wind stress is only 30% of its peak magnitude in the FGGE case. At this time, the wind stress fields are essentially the same in both cases. Contour interval is 0.1 N m^{-2}.

RESULTS

The model is integrated from rest for a period of three years for each case, with the annual wind cycle repeating each year. After the first year of integration, a regular seasonal cycle is established in the model fields. We disregard the first two years of model integration to be sure the seasonal cycle is completely spun up, and present the results from the third year. We concentrate here on the details of the development and decay of the Somali Current system during the SW monsoon in the two cases. Many features in the two cases are similar, and when there are differences, they must of course be related to differences in the two wind fields.

During the NE monsoon, the model Somali Current flows southward along the coast from Socotra to 5°S, where it meets a weak northward flowing current, and both turn offshore and meander into the interior. The northward flowing current in the model is much weaker than its real world counterpart, the EACC, because the model stops at 10°S and therefore only includes a small portion of the Southern Hemisphere tradewinds, which drive the EACC. Therefore, the mechanism of Anderson and Moore (1979) and of Anderson (1981) of inertial overshoot of the EACC causing the early reversal of the

inertial overshoot of the EACC causing the early reversal of the

Somali Current is missing in this model. Still, as early as March 7, in both cases, several weeks before the local winds reverse, there is evidence of northward flow along the coast between 4°S and the equator (Fig. 19). This is due to the relaxation of the alongshore pressure gradient that formed in response to the NE monsoon winds, which reached their peak in mid-January. Similar behavior was reported in a model by Philander and Delecluse (1983). They showed that the pressure gradient force set up by a cross-equatorial wind stress along a western boundary opposes the flow just south of the equator, but is in the same direction as the flow to the north of the equator, so that a relaxation of the wind stress causes a prompt reversal of the flow just south of the equator, but has little effect on the flow to the north of the equator.

Also in Fig. 19, we see an onshore flow at 5°N, that splits at the coast with part flowing to the south and a very weak part to the north. This flow is also found in the MMC case at about 7°N, and is a remnant of the source region of the Somali Current during the NE monsoon, which is moving southward as the wind stress curl patterns change.

By mid-April (Fig. 20), as the winds begin to reverse, a clockwise gyre begins to form south of the equator in the FGGE case, driven by the northwestward extension of the Southern Hemisphere tradewinds. In the MMC case (Fig. 21) the alongshore flow does not

tradewinds. In the MMC case (Fig. 21) the alongshore flow does not

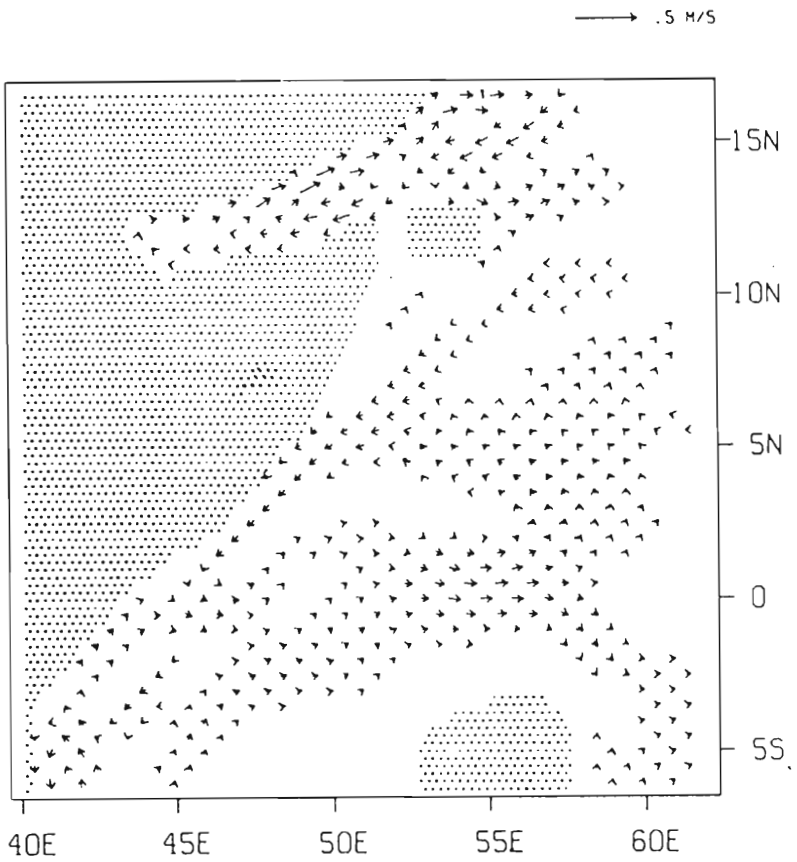

Fig. 19.

Upper layer velocity from the FGGE case for 7 March for the Somali coast region. Arrows indicate speed and direction. Every fourth mesh point is shown. Scale is in upper right-hand corner. Vectors larger than 1.0 ms^{-1} are truncated. Velocities less than 0.03 ms^{-1} are not shown. Northward flow is just beginning along the southern Somali coast, even though the local winds do not reverse for another month. Eastward flow is present along a portion of the equator. There is a band of onshore flow at 5°N, which splits northward and
month. Eastward flow is present along a portion of the equator. There is a band of onshore flow at 5°N, which splits northward and
southward at the coast.

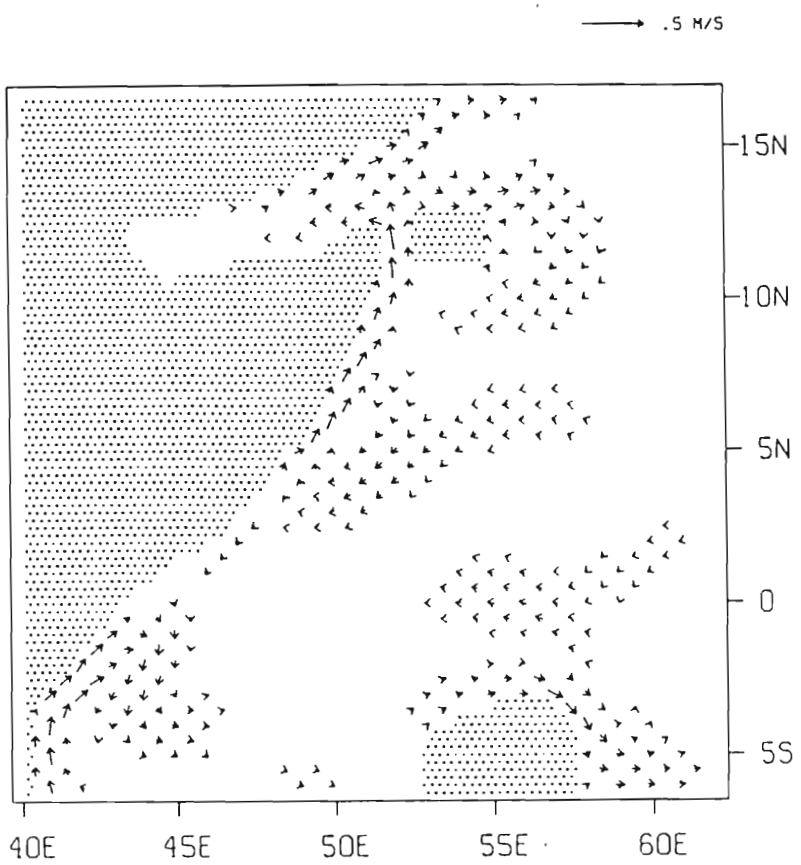

Fig. 20.

Upper layer velocity from the FGGE case for 16 April, as in Figure 19. The winds have just begun to reverse south of the equator, but are primarily onshore north of the equator. There is a gyre-like circulation pattern forming along the coast south of the equator. The onshore flow from the previous month has moved to the south, and feeds a northward flow along the Somali coast between 4°N and the Horn of Africa, with some recirculation at 6°N.

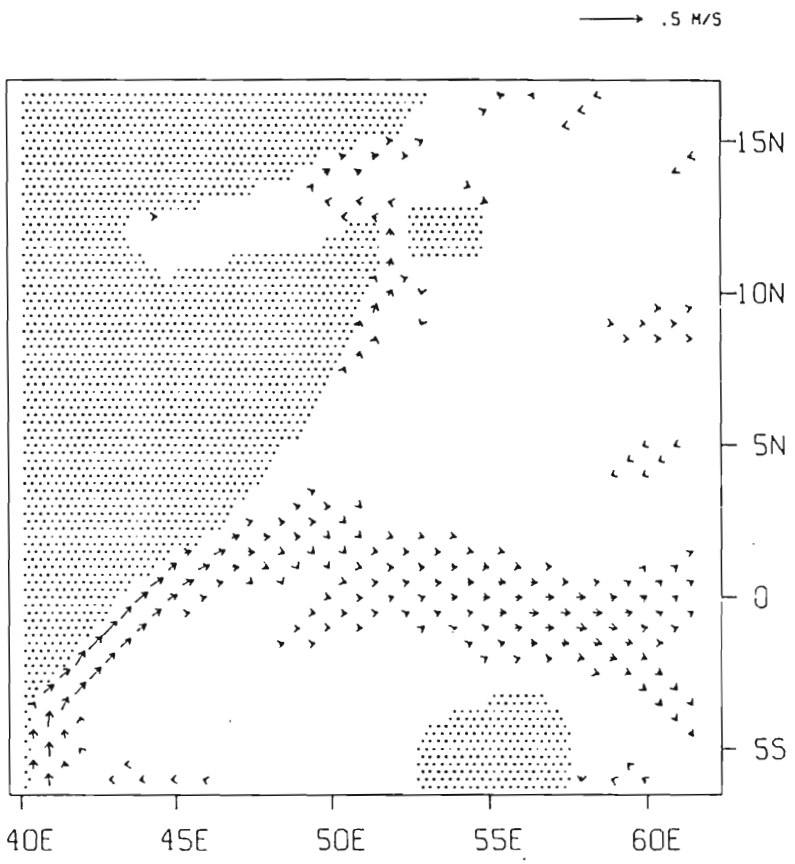

Fig. 21.

Upper layer velocity from the MMC case for 16 April, as in Figure 19. There is northward flow along the Kenya and Somali coasts, but instead of recirculating south of the equator as in the FGGE case, this flow turns eastward along the equator into a broad meandering equatorial current, that is not present in the FGGE case. There is northward flow along the Somali coast between 7°N and 12°N, but it is much weaker than in the FGGE case.

northward flow along the Somali coast between 7°N and 12°N, but it is much weaker than in the FGGE case.

recirculate south of the equator, but feeds into an eastward equatorial current. This equatorial current is driven by the westerly winds along the equator seen in Fig. 5. Both the eastward current and the westerly winds are absent in the FGGE case. A jet similar to this equatorial current was first reported by Wyrtki (1973) during the monsoon transitions and explained theoretically by O'Brien and Hurlburt (1974) as a transient response to the onset of westerly winds. The predicted width of this jet is twice the baroclinic equatorial radius of deformation, or about 500 km. This is in agreement with equatorial current in the MMC case.

The currents north of the equator also differ at this time. In the FGGE case, the winds have a northward component north of 5°N, and drive a northward flow there, while south of 5°N, the winds still have a southward component and drive a weak southward flow there. In the MMC case, only the northward flow is found.

In May, northward flow is found all along the Kenya-Somali coast (Fig. 22 and 23). The Southern Hemisphere flow turns offshore at the equator and recirculates to the south in both cases. This southern gyre is narrower and stronger in the MMC case because the nearshore winds are stronger even though the offshore winds are weaker than in the FGGE case (see Fig. 6 and 7). The equatorial jet in the MMC case is dissipating. There are second offshore turning flows developing in both cases to the north of the equator. In the FGGE case, this flow is between 3°N and 5°N, while in the MMC case,

flows developing in both cases to the north of the equator. In the FGGE case, this flow is between 3°N and 5°N, while in the MMC case,

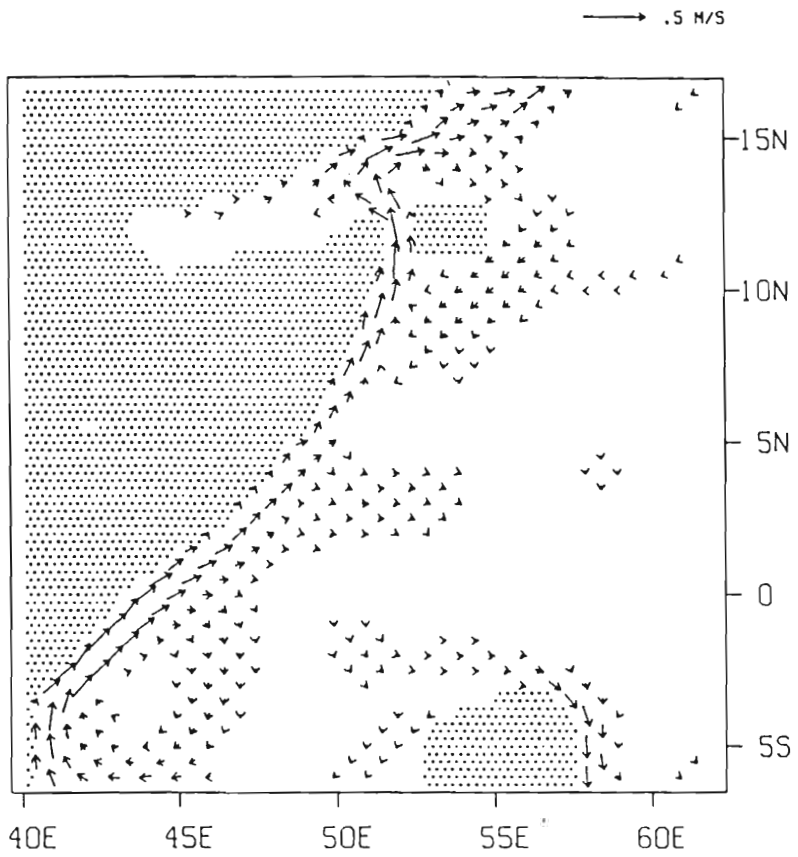

Fig. 22.

Upper layer velocity from the FGGE case for 16 May, as in Figure 19. The gyre south of the equator is now well developed. There is another weak offshore flow developing between 3°N and 5°N. There is northward flow through the channel between Socotra and the Horn of Africa and across the Gulf of Aden, very similar to that inferred from satellite images at this time of the year.

from satellite images at this time of the year.

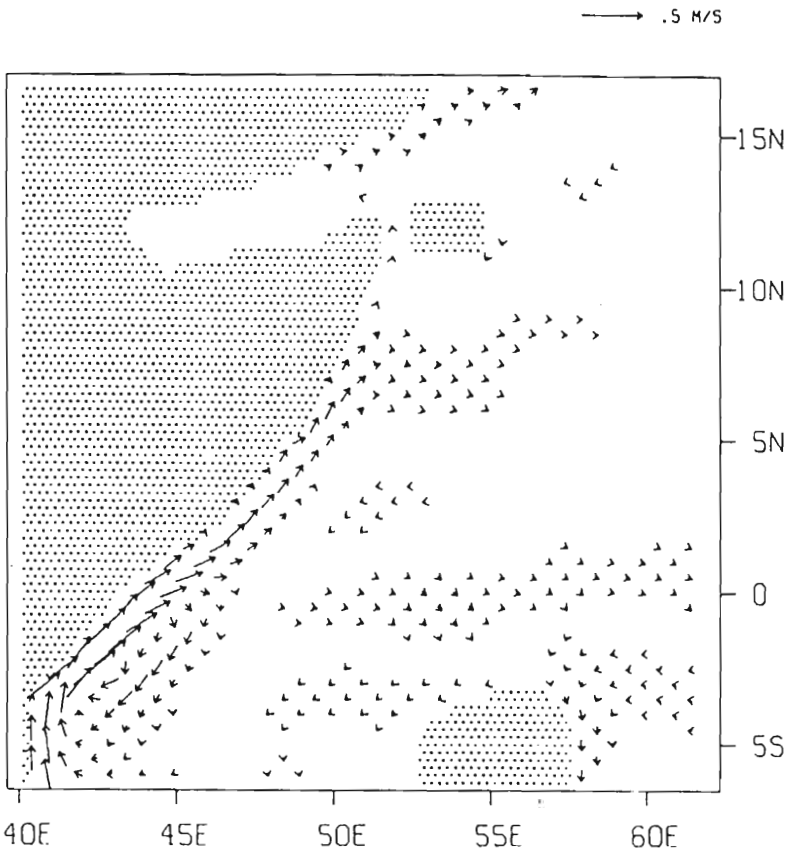

Fig. 23.

Upper layer velocity from the MMC case for 16 May, as in Figure 19. The Southern Hemisphere gyre is tighter, with a larger transport than in the FGGE case. There is a weak offshore flow developing between 6°N and 8°N, with some onshore flow beginning to appear at 3°N, 52°E. This flow will later become the great whirl. There is very little flow through the channel in this case.

very little flow through the channel in this case.

it is between 6°N and 8°N. These latitudes coincide in both cases with the latitude where the Findlater jet moves back offshore, as can be seen in Fig. 6 and 7. Anderson (1981) and Lin and Hurlburt (1981) have suggested that this northern part of the Findlater jet is responsible for generation of the great whirl. As we will see, this offshore flow does develop into the great whirl, but the local (or nearly local) curl of the wind stress is also important, as suggested by Schott and Quadfasel (1983), and by Fig. 8 and 9.

In the FGGE case, the flow along the northern Somali coast passes through the channel between Socotra and the Horn of Africa (Ras Aser or Cape Guardafui, as it is also known) and meanders west and then eastward across the mouth of the Gulf of Aden. Similar flow occurs in the MMC case, but it is much weaker. This behavior has been inferred from satellite infrared imagery and in situ data by B. J. Cagle (personal communication) in early May of 1980. This current appears to be driven by the local wind stress, and controlled by the coastline geometry.

In June the winds increase considerably, and the Findlater jet leaves the coast at 9°N in the FGGE case and 8°N in the MMC case, which is where the maximum wind stress values occur (Fig. 10 and 11). The offshore flow, however, recirculates in a closed gyre centered at 5°N in both cases to form the great whirl (Fig. 24 and 25). This is also the latitude of the relative maximum in negative wind stress curl in both cases (Fig. 12 and 13). The center of

25). This is also the latitude of the relative maximum in negative wind stress curl in both cases (Fig. 12 and 13). The center of

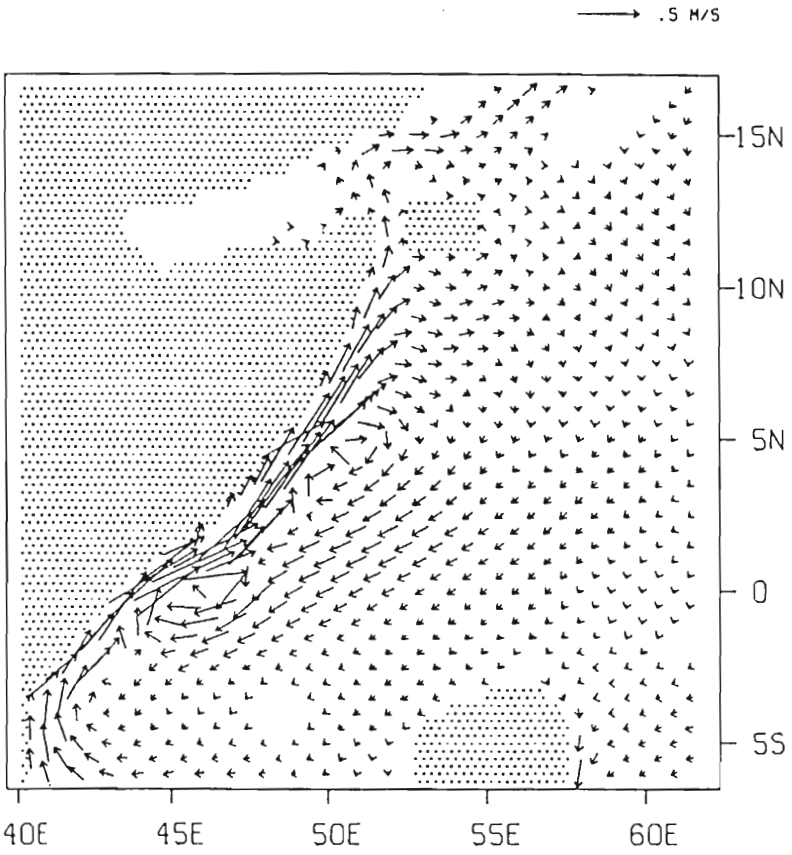

Fig. 24.

Upper layer velocity from the FGGE case for 16 June, as in Figure 19. The offshore flow that was between 3°N and 5°N now extends from 5°N to 10°N. Part of this flow has formed a closed eddy centered at 5°N, to form the beginning of the great whirl of the two gyre circulation. The southern gyre now lies south of 2°N, with a strong recirculation stradling the equator. There is a broad southwestward Sverdrup-like flow farther offshore that crosses the equator and

recirculation stradling the equator. There is a broad southwestward Sverdrup-like flow farther offshore that crosses the equator and

feeds into the southern gyre.

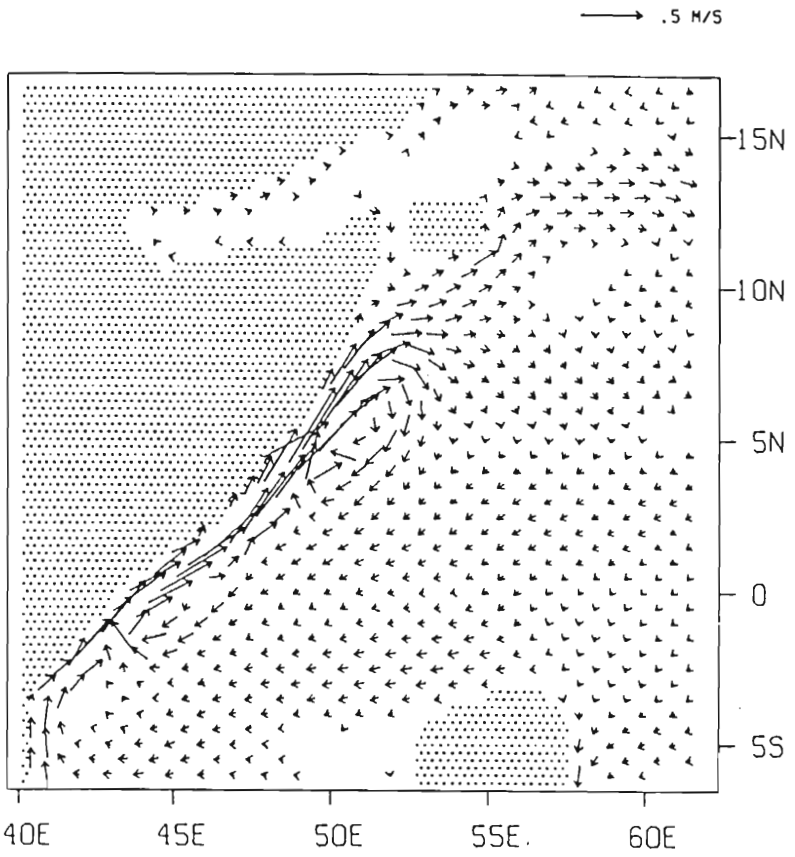

Fig. 25.

Upper layer velocity from the MMC case for 16 June, as in Figure 19. The two gyre circulation pattern develops similarly to the FGGE case, but the current speeds are not as strong. The great whirl forms at about 5°N in both cases. The boundary current separates at a lower latitude in the MMC case, and the flow through the channel is in the opposite direction. In this case, an eastward jet forms along 13°N, fed by outflow from the great whirl. This jet is not seen in the FGGE case.

of these patches is located only 2° to the east of the center of the great whirl, so that the lag time between changes in the curl and changes in the great whirl is very short, especially at this low latitude, and is on the order of a few days.

The southern gyre now turns offshore at 2°N and recirculates southward across the equator. This recirculation is much stronger in the FGGE case because there is much more negative vorticity input by the wind stress curl in this case. In both cases, there is a Sverdrup-like southwestward flow farther offshore that crosses the equator and enters the southern gyre. This flow is stronger in the FGGE case because the negative wind stress curl is stronger.

In the MMC case, outflow from the great whirl passes to the southeast of Socotra and feeds an eastward jet along 13°N (Fig. 25). This jet follows the strong gradient in the wind stress curl along 13°N seen in Fig. 13, and is maintained by the differential Ekman pumping and induced pycnocline slope associated with that gradient (Fig. 26). The curl gradient in the FGGE case (Fig. 12) parallels the Arabian coast and also drives a northeastward current, part of which can be seen at the top of Fig. 24.

By early July, the two gyre system is fully developed. In the FGGE case, the equatorial winds change from westerly to easterly to the east of 60°E (Fig. 10) in early June, and by late June the recirculation region from the southern gyre increases its transport and accelerates northward (Fig. 27). A similar response occurs in recirculation region from the southern gyre increases its transport and accelerates northward (Fig. 27). A similar response occurs in

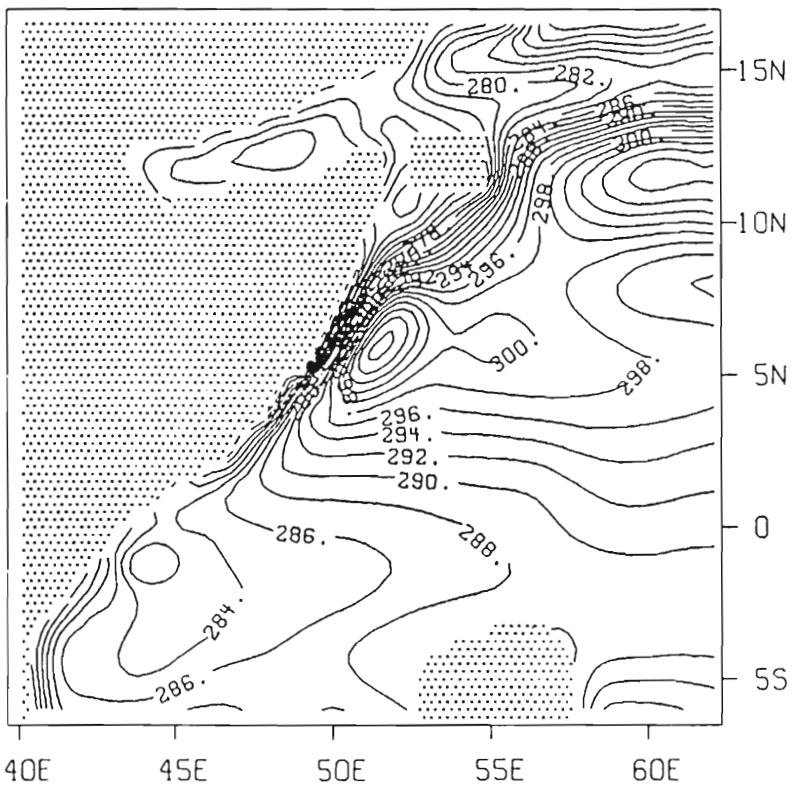

Fig. 26.

Upper layer thickness for 16 June from the MMC case. Note slope along 13°N. Contour interval is 2 m.

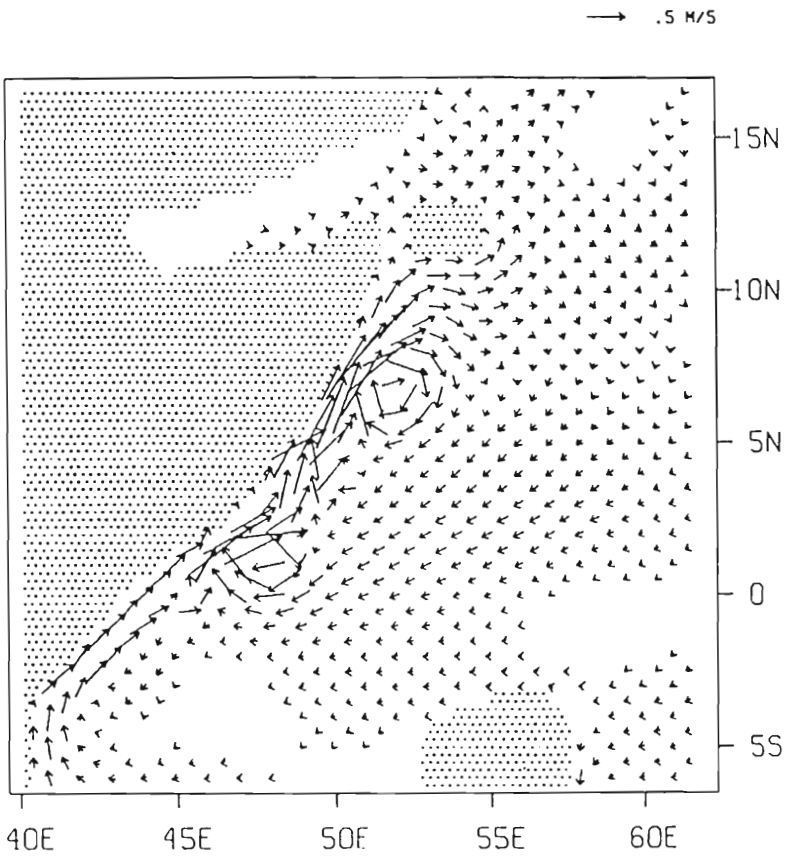

Fig. 27.

Upper layer velocity from the FGGE case for 1 July as in Figure 19. The velocity scale has changed and velocities less than 0.05 ms^{-1} are not shown. The great whirl is fully developed. Flow through the channel has decreased considerably. The recirculation region in the southern gyre is intensifying and is accelerating northward.

the southern gyre is intensifying and is accelerating northward.

the MMC case, but not until mid-July and is triggered by a decrease in the westerly component of the equatorial wind stress. In Fig. 28, the recirculation region is still south of 2°N in the southern gyre on 1 July.

By late July in the FGGE case (Fig. 29), the southern gyre has reached 6°N and is beginning to interact with the great whirl, which is now between 7°N and 12°N. The Northern Hemisphere winds are just beginning to decrease at this time. There is still very little flow from the great whirl passing through the channel.

In the MMC case at this time (Fig. 30), the southern gyre has just begun its northward migration, triggered, it appears, by the decrease in the westerly component of the near-equatorial winds. Another eddy has formed just south of the equator in the southern gyre. To the east of Socotra, another eddy is forming in the outflow from the great whirl and will become the Socotra Eddy.

Between 25 July and 4 August in the FGGE case, we see the southern gyre and the great whirl coalesce (Fig. 31). After the coalescence, there is a more or less continuous boundary current all along the east African coast with some smaller eddies found on its offshore side. The flow through the channel steadily increases, forming an eddy to the north of Socotra. To the east and southeast of Socotra, outflow from the great whirl forms large meanders that will later close into a larger clockwise eddy with a smaller counterclockwise eddy between it and the great whirl.

will later close into a larger clockwise eddy with a smaller counterclockwise eddy between it and the great whirl.

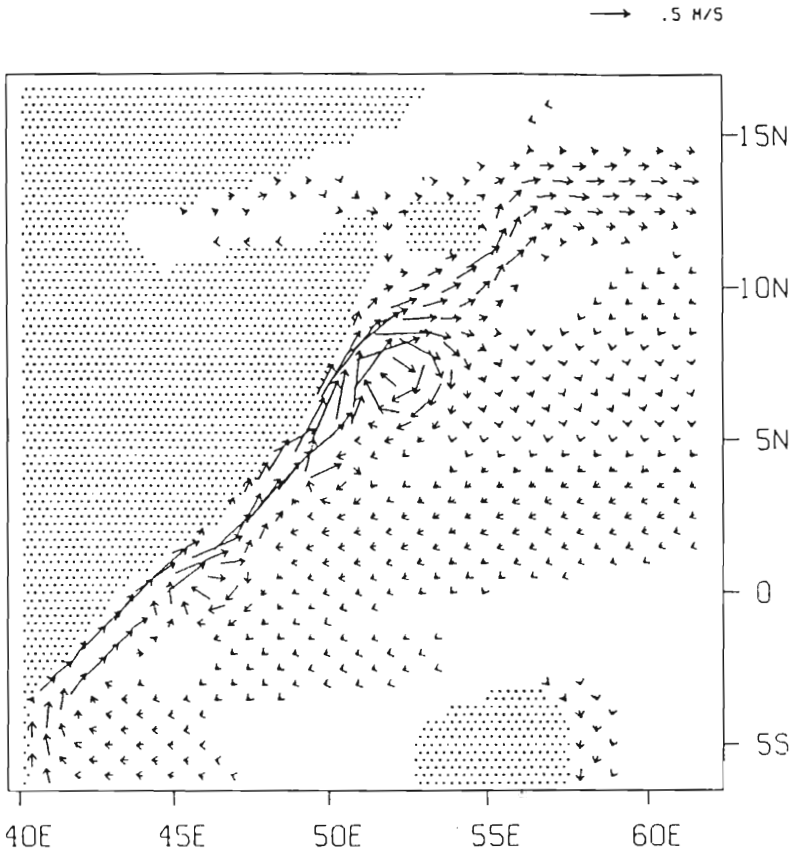

Fig. 28.

Upper layer velocity from the MMC case for 1 July as in Figure 27. The great whirl is well developed and is centered at 7°N. The recirculation region in the southern gyre is not as strong in this case and has not yet begun to accelerate northward, and there is flow from the southern gyre into the great whirl. The eastward jet at 13°N is still present, with no meandering evident.

flow from the southern gyre into the great whirl. The eastward jet at 13°N is still present, with no meandering evident.

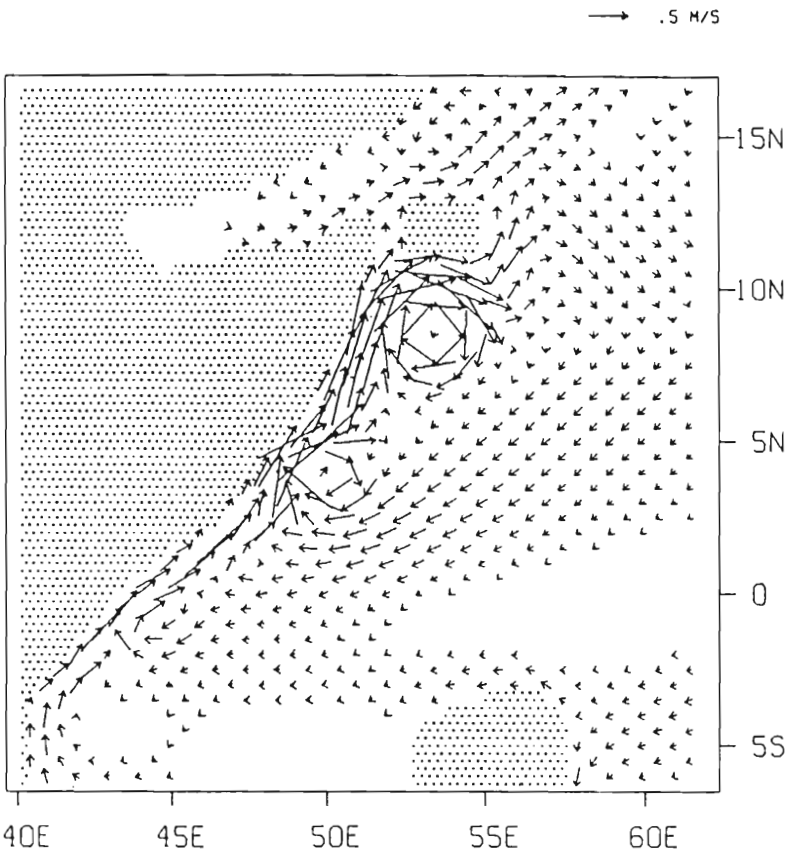

Fig. 29.

Upper layer velocity from the FGGE case for 19 July, as in Figure 27. As the wind stress begins to relax, both the great whirl and the southern gyre are moving northward. There is evidence of a new eddy forming in the southern gyre at the equator.

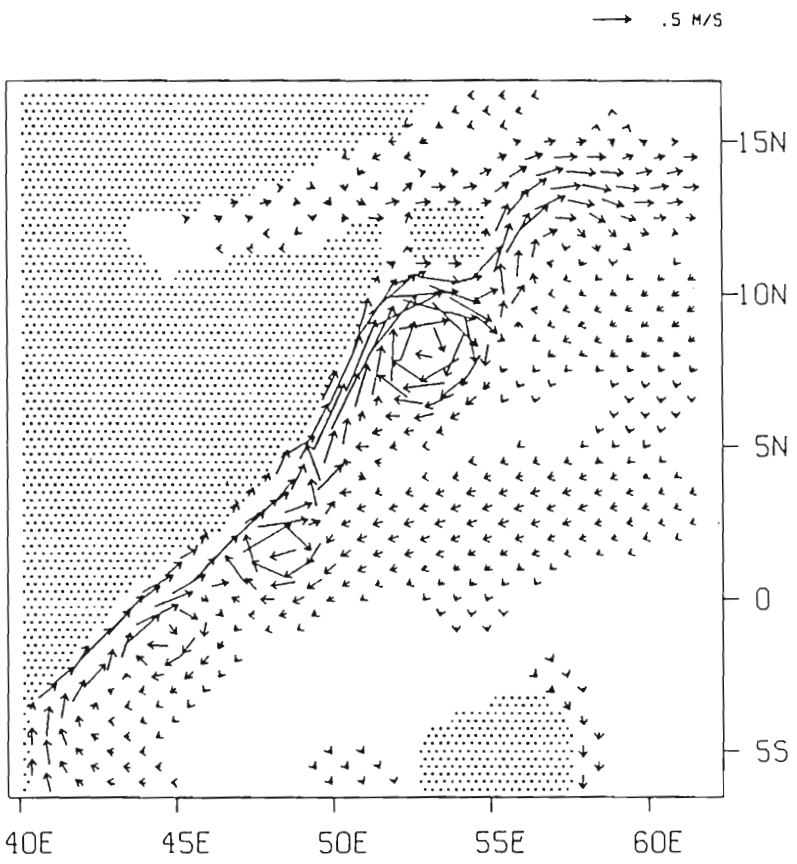

Fig. 30.

Upper layer velocity from the MMC case for 19 July, as in Figure 27. As the winds begin to relax, the recirculation region in the southern gyre intensifies and moves northward. A second eddy has formed in the southern gyre, just south of the equator. The great whirl is now centered at 8°N to 9°N. The outflow from the great whirl is beginning to meander to form the Socotra eddy. Weak eddies are beginning to form to the north of Socotra and in the Gulf of

whirl is beginning to meander to form the Socotra eddy. Weak eddies are beginning to form to the north of Socotra and in the Gulf of

Aden.

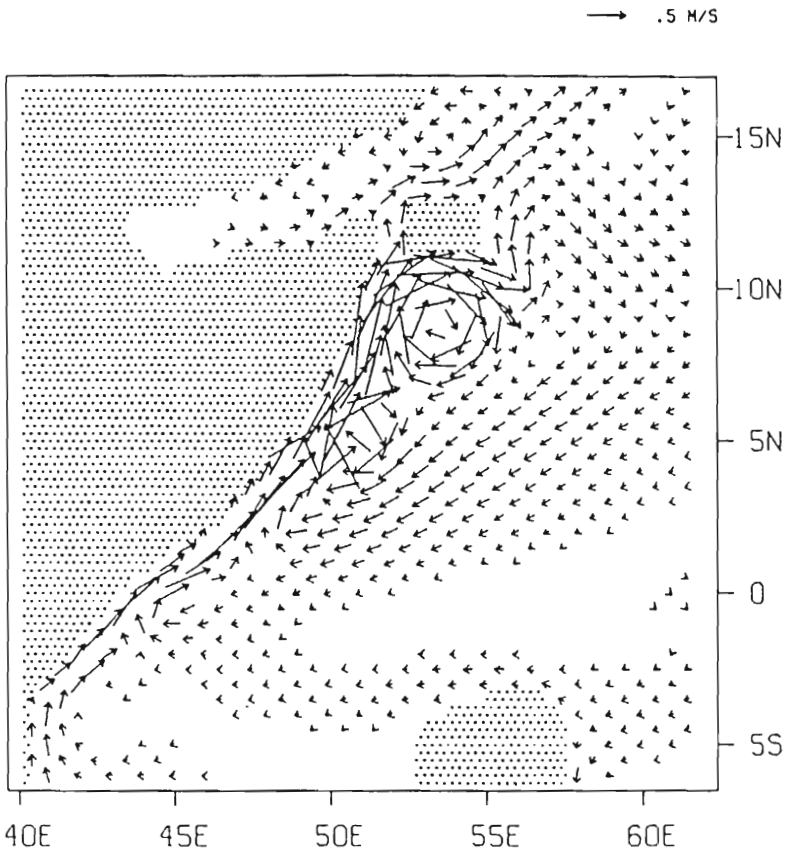

Fig. 31a.

Collapse of the two gyre system in the FGGE case. Upper layer velocity on 25 July. The recirculation region from the southern gyre is beginning to interact with the great whirl. Flow from the great whirl is beginning to pass through the channel. Outflow from the great whirl to the southeast of Socotra is beginning to meander.

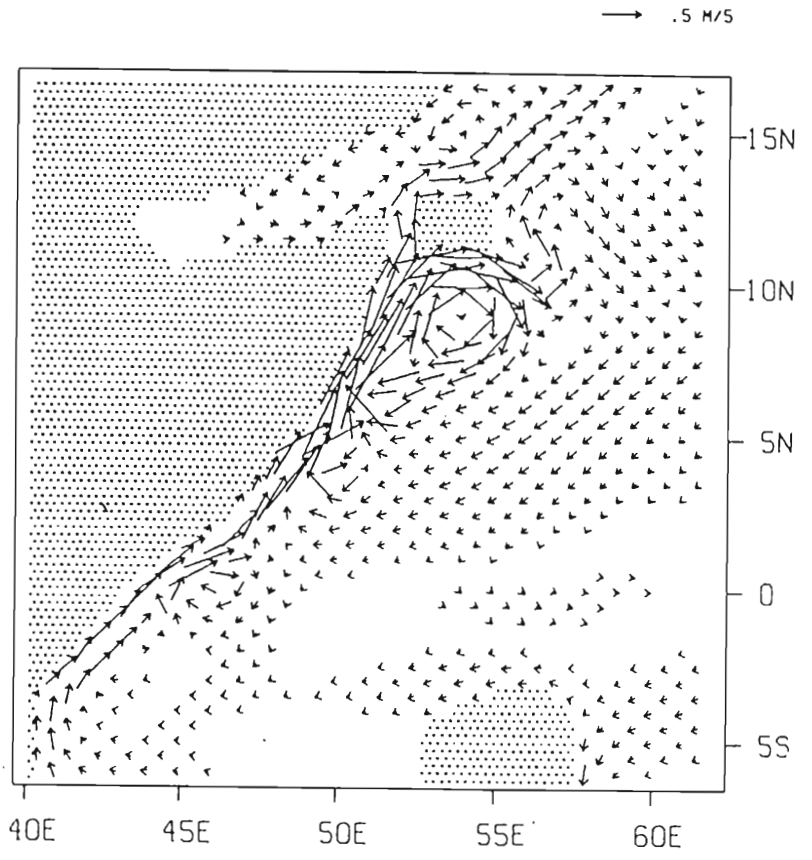

Fig. 31b.

Collapse of the two gyre system in the FGGE case. Upper layer velocity for 1 August. The recirculation region from the southern gyre is coalescing with the great whirl. The flow through the channel and along the north side of Socotra is increasing, and small eddies are forming to the north and west. The outflow from the great whirl to the southeast of Socotra is meandering intensely.

whirl to the southeast of Socotra is meandering intensely.

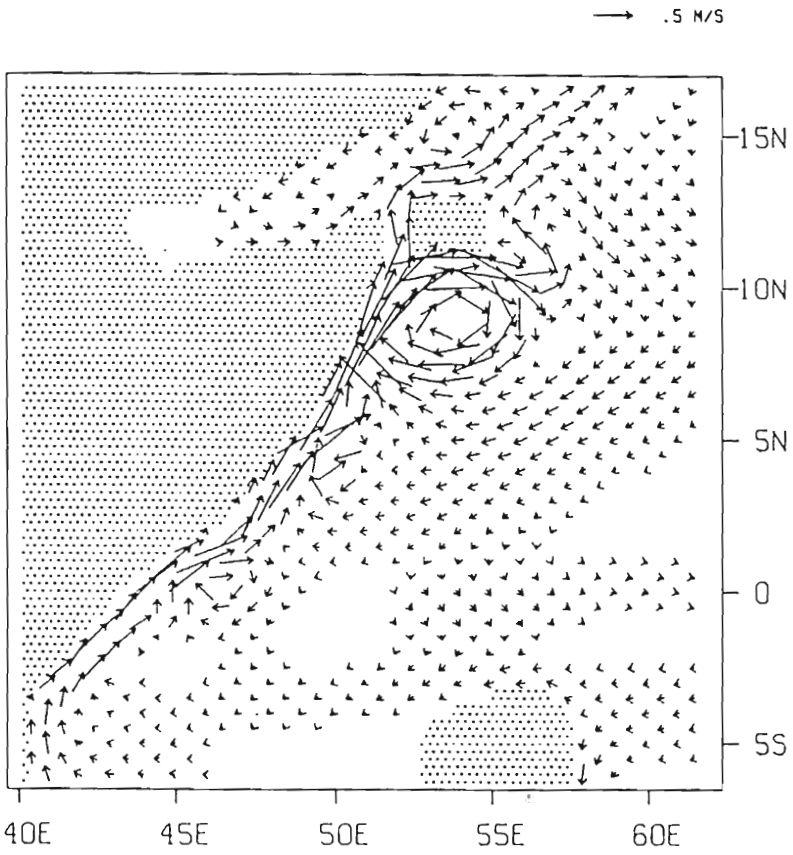

Fig. 31c.

Collapse of the two gyre system in the FGGE case. Upper layer velocity for 4 August. The recirculation region from the southern gyre has completely merged with the great whirl. Closed eddy circulations are forming in the meandering outflow from the great whirl to the southeast of Socotra. The eddy at the equator is strengthening, as are the eddies to the north and west of Socotra.

are the eddies to the north and west of Socotra.

The coalescence of the southern gyre and the great whirl occurs in the MMC case between 19 and 28 August (Fig. 32), in much the same manner as in the FGGE case. A prominent eddy forms at the equator in this case, with significant offshore flow just north of the equator. In the FGGE case, only a small eddy forms at the equator at this time, but it is mostly confined to the offshore edge of the current. This difference can be explained by the difference in strength of the Southern Hemisphere winds, which are much weaker in the MMC case. The boundary current is not as strong, and does not have enough inertia to overcome its tendency to turn offshore north of the equator.

As the wind stress curl gradient relaxes in August and September, the pressure gradient that was maintained by the differential Ekman suction becomes unbalanced. As this forcing is removed, more and more of the great whirl flow passes through the channel, until by October, there is a clockwise flow around the island of Socotra (Fig. 33). The southern part of this flow will become the source of the NE monsoon Somali current. Southward flow steadily overrides the northward flow, pushing it to 5°S by late November or early December.

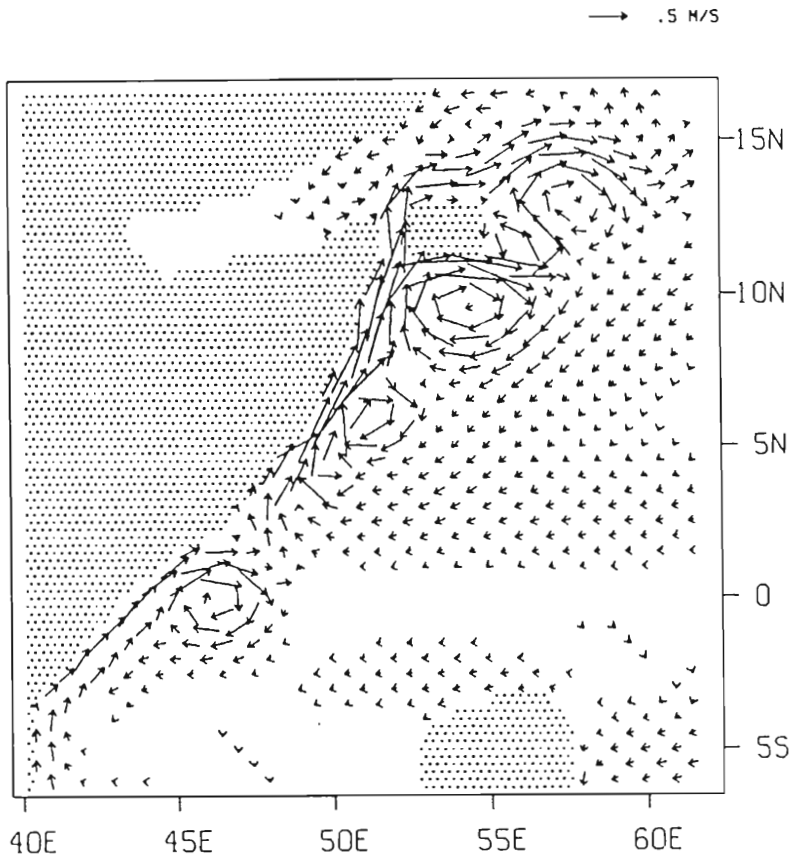

Fig. 32.

Upper layer velocity from the MMC case for 19 August. The coalescence of the great whirl and the southern gyre is just beginning at this time, much later than in the FGGE case. The Socotra eddy is fully developed to the east of Socotra, with a small cyclonic circulation between it and the great whirl. There is a large eddy located at the equator, with considerable offshore flow to the north of it, so that there is not a continuous boundary current all along the coast. This situation persists until the onset of the northeast monsoon. Otherwise, the collapse of the two gyre system in this case proceeds much the same as in the FGGE case.

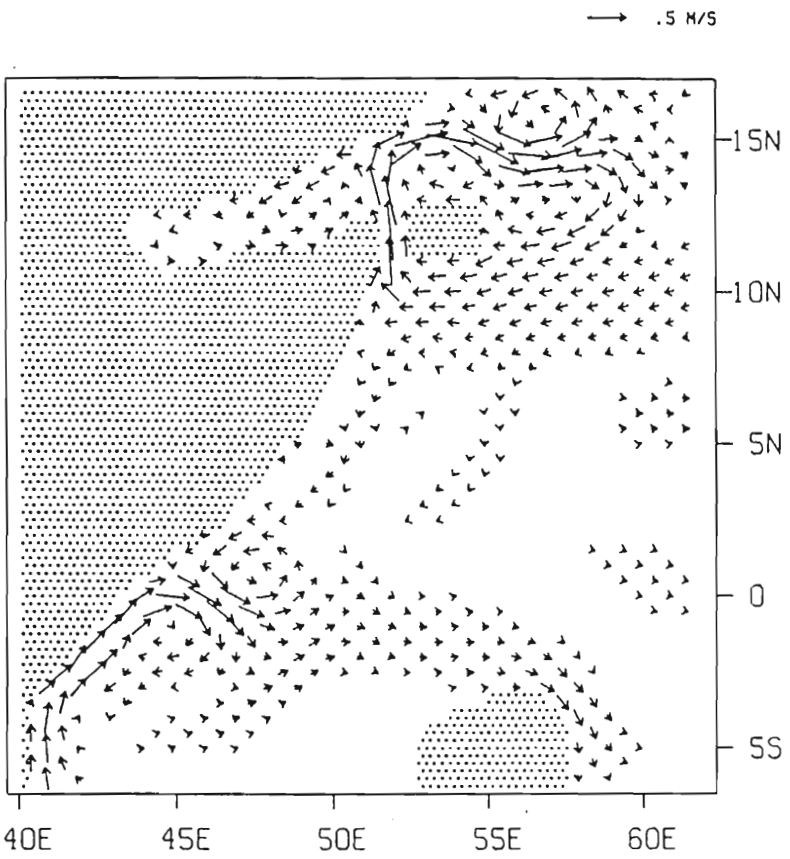

Fig. 33.

Upper layer velocity from the MMC case for 16 October. The great whirl flow has been completely forced through the channel, due to the relaxation of the wind stress curl gradient, so that there is now a clockwise circulation around the island of Socotra. The southern part of this circulation becomes the source of the southward flowing winter Somali current.

southern part of this circulation becomes the source of the southward flowing winter Somali current.

DISCUSSION AND CONCLUSION

By comparing the results of this model for these two separate cases, we can draw some conclusions about the relative importance of the different forcing mechanisms in the generation and decay of the two gyre system in the Somali Current. Figure 34 (a and b) summarizes the development and collapse of the two gyre system by showing the northward component of transport across 2° zonal sections following the coast with time and distance. The minimum in northward transport along lines A and B indicates the separation between the southern gyre and the great whirl. The southern gyre recirculation region forms in early May in each case. Its center is indicated by the relative maximum along lines C and D. It moves very slowly northward through May and June. During this period, the separation region remains at about 2°N. In early June, the great whirl forms between 4°N and 8°N, and steadily increases its transport. In late June in the FGGE case and mid July in the MMC case, the separation region abruptly begins to move northward, as the recirculation dramatically increases its transport and its northward speed. Both move northward at an average speed of 25 km/day in the FGGE case (18 km/day in the MMC case). The northward migration of the separation region (the relative minimum along line B) can be interpreted as the northward movement of the cold wedge

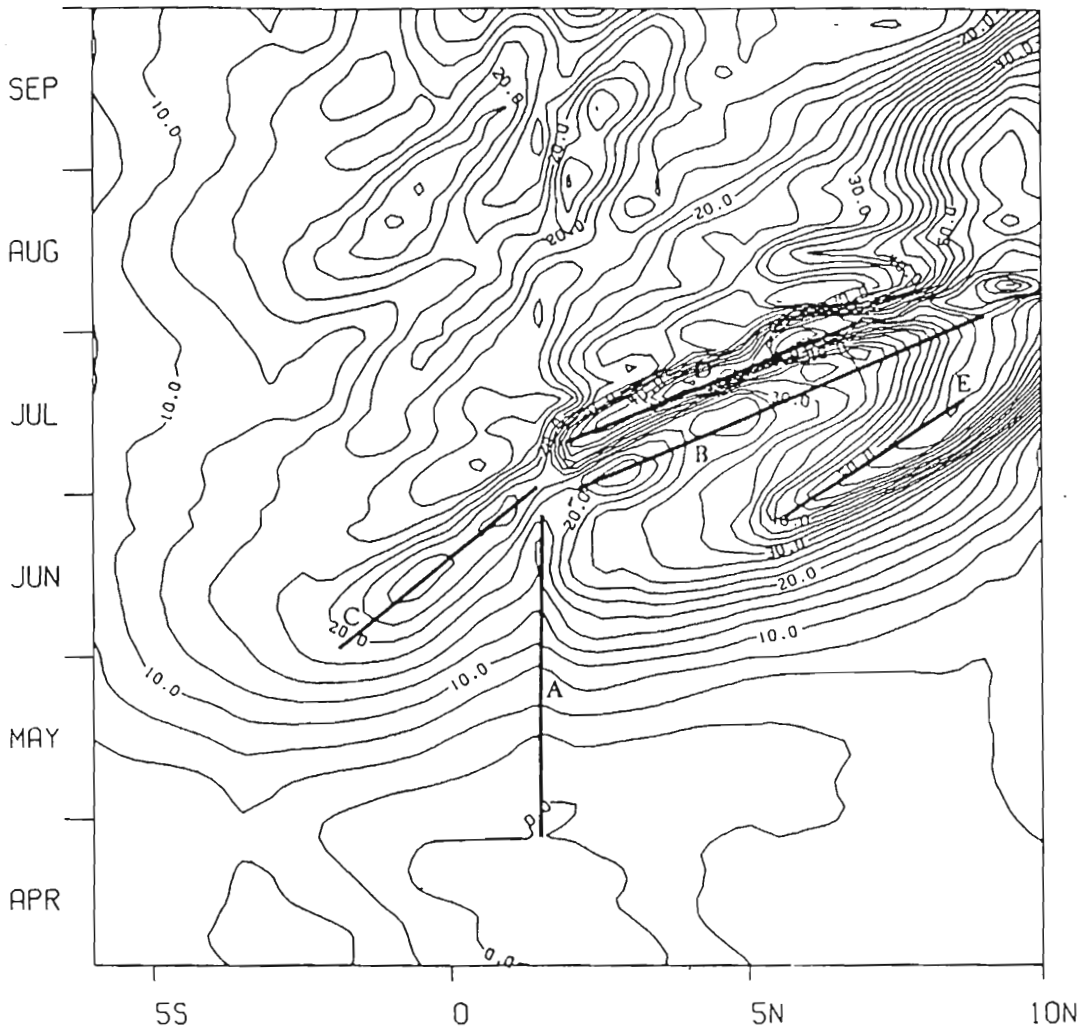

Fig. 34a.

Northward component of transport across sections following the coast vs time and latitude for the FGGE case. Lines A and B follow the separation region between the southern and northern gyre. Lines C and D follow the center of the southern gyre recirculation region. Line E follows the northward movement of the great whirl. Units are 10^6 m^3 s^{-1}. Contour interval is 10 x 10^6 m^3 s^{-1}.

Line E follows the northward movement of the great whirl. Units are 10^6 m^3 s^{-1}. Contour interval is 10 x 10^6 m^3 s^{-1}.

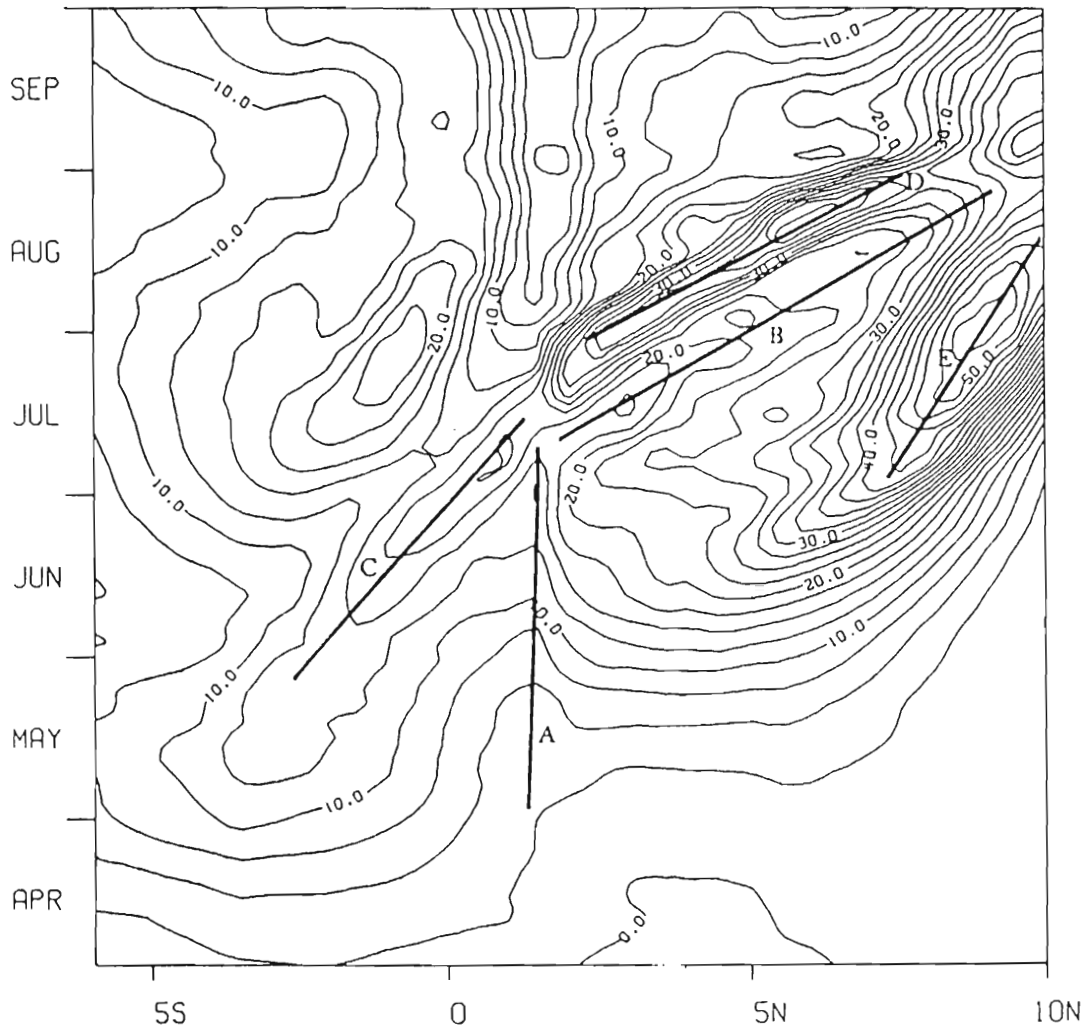

Fig. 34b.

Northward component of transport across sections following the coast vs time and latitude for the MMC case. Lines A and B follow the separation region between the southern and northern gyre. Lines C and D follow the center of the southern gyre recirculation region. Line E follows the northward movement of the great whirl. Units are 10^6 m^3 s^{-1}. Contour interval is 10 x 10^6 m^3 s^{-1}.

10^6 m^3 s^{-1}. Contour interval is 10 x 10^6 m^3 s^{-1}.

observed in satellite images by Brown et al. (1980), Evans and Brown (1981) and Swallow et al. (1983). As the southern gyre approaches the great whirl, it also moves northward, although much more slowly, as it is confined by Socotra to the north. In late July in the FGGE case (late August in the MMC case) the southern gyre catches the great whirl, and the two coalesce. This is observed in satellite images as a coalescence of the southern cold wedge with a northern cold wedge.

The question remaining is what triggers the northward migration of the southern gyre? The large increase in transport occurs only in the recirculation region as it moves away from the equator and not to the south. As its transport increases, its self advection speed also increases. This transition occurs at northward transport values of about 30×10^6 $m^3 s^{-1}$ in the FGGE case and 20×10^6 $m^3 s^{-1}$ in the MMC case. This seems to rule out the idea that the steadily increasing transport reaches some critical value after which it becomes unstable and advects northward, as was suggested in several other models (e.g., Hurlburt and Thompson, 1976; Cox, 1976, 1979; Lin and Hurlburt, 1981). The northward movement coincides with a decrease in the westerly component of the winds along the equator in both cases, although this occurs at different times in each case. This certainly points to something in the wind field triggering the northward movement. If the winds along the equator have a westerly component that decreases or even changes to easterly, this will send

northward movement. If the winds along the equator have a westerly component that decreases or even changes to easterly, this will send

a stream of downwelling Rossby wave energy westward that will quickly reach the western boundary and cause a convergence of mass there. This convergence would intensify the recirculation region of the southern gyre and cause it to accelerate northward through nonlinear self advection. In the FGGE case, the convergence zone in the winds crosses the equator around 1 June, causing the equatorial winds to shift from westerly to easterly to the east of 60°E. It would take a first mode equatorial Rossby wave approximately 20 days to travel from 60°E to the Somali coast, which is consistent with timing of the northward acceleration of the southern gyre. In the MMC case, the winds all across the equator have a westerly component. As these westerly winds decrease in mid-July, downwelling Rossby wave energy almost immediately reaches the Somali coast, since it is generated all along the equator. This again is consistent with the increase in transport of the southern gyre occuring in mid-July.

Also from Figure 34 we can see that the southern gyre in the FGGE case moves northward faster because its transport is about 25% larger than in the MMC case. Its translation speed also increases slowly as its transport increases.

We have shown that the spatial and temporal inhomogeneity of the winds play a crucial role in the development of the Somali Current system. The pre-monsoon onset conditions are important in determining the early current reversals. The relaxation of the NE

Current system. The pre-monsoon onset conditions are important in determining the early current reversals. The relaxation of the NE monsoon winds is sufficient to cause the currents to reverse south

of the equator, so that the mechanism of early forcing by the Southern Hemisphere tradewinds, which are not included in this model, is not necessary. This is not to say that forcing by the Southern Hemisphere tradewinds is not important. Our EACC is very weak or non-existent at times because of their absence. The tradewinds do come far enough north later in the SW monsoon that they become important in our model. Anderson and Moore (1979) showed that it is the curvature of the wind near the equator that is important in determining the separation point of the southern gyre, but that this is modified by the inertial effects. Perhaps our southern gyre would penetrate farther north if we had resolved more of the Southern Hemisphere tradewinds.

It appears that the wind stress curl is as important in the development of the great whirl as is the local wind stress. As Anderson (1981) and Lin and Hurlburt (1981) showed, the great whirl can be generated by the alongshore winds associated with the Findlater jet as it crosses the Somali coast at about 9°N, without the presence of a wind stress curl. Anderson (1981) found that the center of this northern gyre, and hence the maximum alongshore velocities, were located at the same latitude as the maximum longshore winds, while Lin and Hurlburt (1981) found that the gyre forms just south of the wind maximum. Their model winds also included a significant curl in the vicinity of the gyre development. In our model the center of the great whirl is located at the same

In our model the center of the great whirl is located at the same

latitude as the maximum negative wind stress curl throughout June and early July, while the maximum wind stress is located farther to the north. The negative vorticity input by the wind stress curl appears to control the location of the great whirl in both cases.

The mechanism of forcing by the differential Ekman pumping associated with the strong gradients in wind stress curl has not, to our knowledge, been reported elsewhere, and requires further investigation. It appears to be important in the formation of both the great whirl and the jet at 13°N. Compare for instance Figure 13 and 26. The strong gradients in upper layer thickness closely parallel the gradients in wind stress curl. The relaxation of this forcing is also important in the formation of the Socotra eddy and in the movement of the great whirl flow through the channel.

The results of this model have been very encouraging this far. We are in the process of extending the model to include the entire Indian Ocean north of 25°S so that we may include the effects of the Southern Hemisphere tradewinds and the equatorial wave guide east of 73°E. We are also studying the differential Ekman pumping mechanism. How sensitive is it to the parameterization of the wind stress as the body force over the upper layer? How does the relaxation of this forcing generate the eddies observed in the model? Might we expect this mechanism to be important in other areas of the world where the curl gradients are not as strong? We hope to report progress in these areas in the near future.
areas of the world where the curl gradients are not as strong? We hope to report progress in these areas in the near future.

REFERENCES

ANDERSON, D. L. T. (1981) The Somali Current. Ocean Modelling (unpublished manuscript).

ANDERSON, D. L. T. and D. W. MOORE (1979) Cross-equatorial jets with special relevance to very remote forcing of the Somali Current. Deep-Sea Research, 26, 1-22.

BENGTSSON, L., J. KANAMITSU, P. KALLBERG AND S. UPPALA (1982) FGGE 4-dimensional data assimilation at ECMWF. Bulletin American Meteorological Society, 63, 29-43.

BROWN, O. B., J. G. BRUCE and R. H. EVANS (1980) Evolution of sea surface temperature in the Somali Basin during the southwest monsoon of 1979. Science, 209, 595-597.

BRUCE, J. G. (1973) Large scale variations of the Somali Current during the southwest monsoon, 1970. Deep-Sea Research, 20, 837-846.

BRUCE, J. G. (1979) Eddies off the Somali coast during the southwest monsoon. Journal of Geophysical Research, 84, C12, 7742-7748.

BRUCE, J. G. (1983) The wind field in the western Indian Ocean and the related ocean circulation. Monthly Weather Review, 111, 1442-1452.

CAMERLENGO, A. L. and J. J. O'BRIEN (1980) Open boundary conditions in rotating fluids. Journal of Computational Physics, 35, 12-35.

CHARNEY, J. G. (1955) The generation of ocean currents by the wind. Journal of Marine Research, 14, 477-498.

CHARNEY, J. G. (1955) The generation of ocean currents by the wind. Journal of Marine Research, 14, 477-498.

COX, M. D. (1976) Equatorially trapped waves and the generation of the Somali Current. Deep-Sea Research, 23, 1139-1152.

COX, M. D. (1979) A numerical study of Somali Current eddies. Journal of Physical Oceanography, 9, 311-326.

EVANS, R. H. AND O. B. BROWN (1981) Propagation of thermal fronts in the Somali Current system. Deep-Sea Research, 28, 521-527.

FINDLATER, J. (1971) Mean monthly airflow at low levels over the western Indian Ocean. Geophysical Memoirs, no. 115, 53 pp.

FINDLAY, A. G. (1866) A directory for the navigation of the Indian Ocean. Richard Holmes Laurie, London, 1062 pp.

HASTENRATH, S. and P. J. LAMB (1979) Climate atlas of the Indian Ocean. University of Wisconsin Press, Madison.

HELLERMAN, S. and M. ROSENSTEIN (1983) Normal monthly wind stress over the world ocean with error estimates. Journal of Physical Oceanography, 13, 1093-1104.

HURLBURT, H. E. (1974) The influence of coastline geometry and bottom topography on the eastern ocean circulation. Ph.D. dissertation, Florida State University, 104 pp.

HURLBURT, H. E. and J. D. THOMPSON (1976) A numerical model of the Somali Current. Journal of Physical Oceanography, 6, 646-664.

KNOX, R. A. and P. L. T. ANDERSON (1984) Recent advances in the study of the low-latitude ocean circulation. Progress in Oceanography (in press).

LEETMAA, A. (1972) The response of the Somali Current to the southwest monsoon of 1970. Deep-Sea Research, 19, 319-325.

LEETMAA, A. (1972) The response of the Somali Current to the southwest monsoon of 1970. Deep-Sea Research, 19, 319-325.

LEETMAA, A., D. R. QUADFASEL, and D. WILSON (1982) Development of the flow field during the onset of the Somali Current, 1979. Journal of Physical Oceanography, 12, 1325-1342.

LIN, L. B. and H. E. HURLBURT (1981) Maximum simplification of nonlinear Somali Current dynamics. Monsoon Dynamics, M. J. Lighthill and R. P. Pearce, editor, Cambridge University Press.

LUTHER, M. E. and J. J. O'BRIEN (1984) A model of the seasonal circulation in the Arabian Sea forced by observed winds. Progress in Oceanography, (in press).

O'BRIEN, J. J. and H. E. HURLBURT (1974) Equatorial jet in the Indian Ocean: Theory. Science, 184, 1075-1077.

PHILANDER, S. G. H. and P. DELECLUSE (1983) Coastal currents in low latitudes. Deep-Sea Research, 30, 887-902.

SCHOTT, F. (1983) Monsoon response of the Somali Current and associated upwelling. Progress in Oceanography, 12, 357-382.

SCHOTT, F. and D. R. QUADFASEL (1982) Variability of the Somali Current system during the onset of the southwest monsoon, 1979. Journal of Physical Oceanography, 12, 1343-1357.

SWALLOW, J. C. and M. FIEUX (1982) Historical evidence for two gyres in the Somali Current. Journal of Marine Research, 40, supplement, 747-755.

SWALLOW, J. C., R. L. MOLINARI, J. G. BRUCE, O. B. BROWN and R. H. EVANS (1983) Development of near-surface flow pattern and water mass distribution in the Somali Basin, in response to the southwest monsoon of 1979. Journal of Physical Oceanography, 13, 1398-1415.

WYRTKI, K. (1973) An equatorial jet in the Indian Ocean. Science, 181, 262-264.

WYRTKI, K. (1973) An equatorial jet in the Indian Ocean. Science, 181, 262-264.